

Unifying supervised learning and VAEs - automating statistical inference in (astro-)particle physics with amortized conditional normalizing flows

Thorsten Glüsenkamp*

*Erlangen Centre for Astroparticle Physics (ECAP),
Friedrich-Alexander Universität Erlangen-Nürnberg,
Erlangen, Germany*

August 16, 2022

Abstract

A KL-divergence objective of the joint distribution of data and labels allows to unify supervised learning and variational autoencoders (VAEs) under one umbrella of stochastic variational inference. The unification motivates an extended supervised scheme which allows to calculate a goodness-of-fit p-value for the neural network model. Conditional normalizing flows amortized with a neural network are crucial in this construction. We discuss how they allow to rigorously define coverage for posteriors defined jointly on a product space, e.g. $\mathbb{R}^n \times \mathcal{S}^m$, which encompasses posteriors over directions. Finally, systematic uncertainties are naturally included in the variational viewpoint. In classical likelihood approaches or other machine learning models, the ingredients of (1) systematics, (2) coverage and (3) goodness-of-fit are typically not all available or at least one of them strongly constrained. In contrast, the proposed extended supervised training with amortized normalizing flows accommodates all three of them for variational inference of arbitrary statistical distributions defined on product spaces like $\mathbb{R}^n \times \dots \times \mathcal{S}^m$ and no fundamental barrier in terms of complexity of the underlying data. It therefore has great potential for the statistical toolbox of the contemporary (astro-)particle physicist.

Contents

1	Introduction	2
2	Monte Carlo estimates and the joint KL-divergence	3
2.1	Supervised learning	4
2.2	Unsupervised learning: Variational autoencoders	5
2.3	Extended supervised and semi-supervised learning	7
3	Toy Monte Carlo	9
4	The importance of flow-based models	11
5	Systematic Uncertainties	14
6	Coverage of the neural network posterior	14
7	Goodness-of-Fit of the neural network model	16
8	Related Work	20
9	Conclusion	21
A	Supplementary material for goodness-of-fit simulation	22

*thorsten.gluosenkamp@fau.de

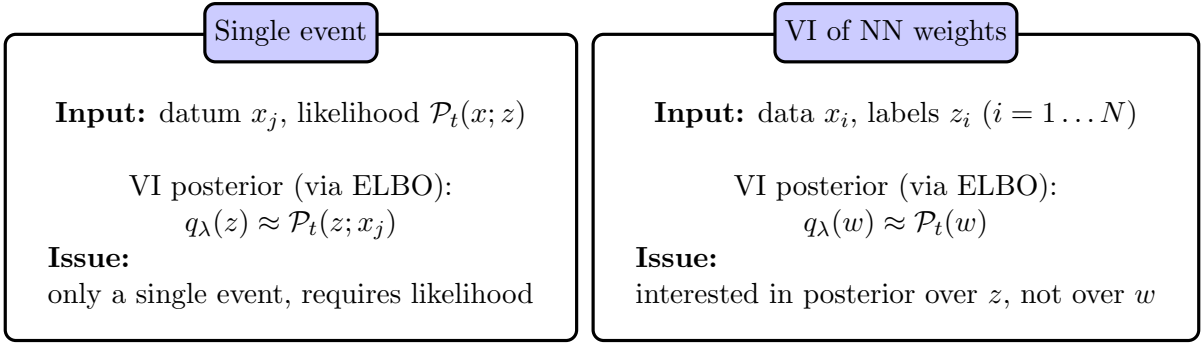
B Implementation details	22
B.1 Training	22
B.2 Posterior	24
B.3 Likelihood	24
B.4 Parameter choices	24
C Coverage for spheres	24

1 Introduction

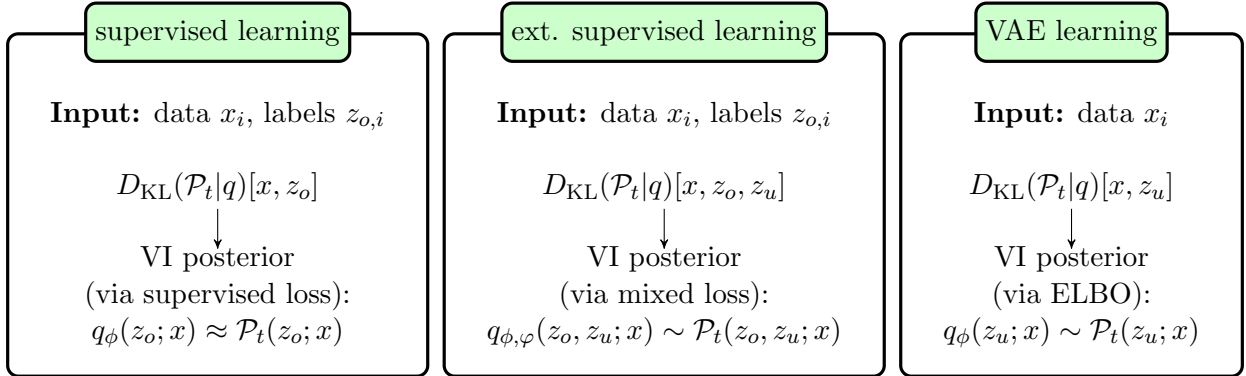
Deep neural networks have achieved great results over the last couple of years. While the breakthroughs were initially made in industrial applications, for example in image processing [1], in recent years their application in fundamental science has become more and more ubiquitous. A typical application of deep learning in experimental high-energy physics is concerned with the reconstruction of particle interactions [2]. These include discrete quantities like particle type [3] or continuous quantities like direction, position and energy [4]. Traditionally, reconstructions of continuous quantities are performed by parametrized likelihood fits [5] which allow to calculate confidence intervals with standard Frequentist or Bayesian methods [6]. Neural networks on the contrary are often used to produce point estimates [7], and there is no universal agreed-upon notion how to calculate confidence intervals. Often they are just ignored, the result is registered as an observable and used in a binned likelihood analysis [4]. Per-event uncertainties are not necessarily required for this use-case. However, there are many situations where precise uncertainty quantification is important. An example are per-event reconstructions in high-energy neutrino telescopes like IceCube [8] or gravitational-wave observatories like LIGO [9] in the context of multi-messenger astronomy [10]. These experiments send out alerts to the astronomical community to perform follow-up observations with other experiments. On the one hand, these alerts are time-critical and should be sent out to the public as fast as possible. On the other hand, the uncertainties of the inferred direction must be precise and in particular not biased. While the time-critical aspect of this use-case is in favor of neural networks, obtaining unbiased uncertainties can be a challenge. A naive solution could employ Bayesian neural networks [11] or approximations like certain dropout-variations [12] or ensemble-methods [13]. However, these methods model a posterior over network weights, not over the actual physics parameters. An alternative is to parametrize the likelihood function with a neural network and perform a standard likelihood-based Frequentist or Bayesian analysis. Recently, this was done for gravitational-wave signals with flow-based networks [14]. Such methods, however, inherit the disadvantages of likelihood-based inference. They can be fall into local optima during an optimization routine or have potentially long running times when Markov Chain Monte Carlo [15] (MCMC) is used to obtain samples. An alternative that recently has gotten popular is likelihood-free inference with neural networks, in which the posterior is directly learned from data. This has been applied to gravitational wave posteriors modeling the posterior as a parametrized Gaussian or mixture of Gaussians [16] and going beyond to use autoregressive normalizing flows for more complex shapes [17]. This paper is about the same line of thinking, where the posterior or more generally parts of the joint distribution of data and labels are learnt using normalizing flows.

We first discuss that the training process in supervised learning can be recast as variational inference of the true posterior distribution over labels, where the variational approximation is parametrized by a neural network. The derivation involves the Kullback-Leiber (KL)-divergence [18] of the joint distribution of data and labels. This is a known derivation and the final loss function is sometimes called "conditional maximum-likelihood objective" in the machine learning literature [19]. While the loss indeed represents a likelihood with respect to the neural network parameters, we emphasize it is more useful to think of it as an approximation of the posterior over the latent variables. Standard supervised learning usually uses the mean-squared-error (MSE) loss function, which corresponds to a standard-normal posterior as an approximation of the true posterior. This can often be a bad approximation. We compare it to the slightly more complex case of a Gaussian with a single covariance parameter and in particular approximations based on normalizing flows [20], which in principle have arbitrary approximation capabilities. Since all Gaussian approximations, including the basic MSE loss, can be thought of as special cases of normalizing flows, so-called *affine flows*, it seems sensible to view all supervised loss functions from this angle. While normalizing-flow base distributions can be arbitrary, it turns out that there are advantages of starting with a standard normal as a base distribution that go beyond the argument of simple evaluation. The standard normal automatically allows for straightforward coverage tests, which are discussed in Section 6.

Usually, variational inference with neural networks is employed in unsupervised learning in the context of variational autoencoders (VAEs). As we will show (Section 2.2), one can derive the Evidence Lower Bound (ELBO) [21] of a variational autoencoder from the same joint KL-divergence as the supervised "maximum likelihood objective". This new derivation not only explicitly indicates how supervised learning and VAE training is connected, but it also sheds some light on the interpretation of VAEs. Importantly, we use this connection to motivate a mixed training scheme which we call "extended supervised" learning (Section 2.3). This which allows to calculate Bayesian goodness-of-fit values (Section 7) for the trained model. Figure 1 indicates an overview of the resulting picture. Traditional variational inference (Fig. 1 a) is typically



(a) Two examples of "classical" variational inference. The variational parameters are denoted by λ .



(b) Three examples of "explicit" variational inference of the posterior in target space z , unified by the joint KL-divergence as outlined in Section 2. The label (z_o - "observed") and latent (z_u - "unobserved") variables correspond to physical parameters in high-energy physics. For the latent variables, this is only true up to an identifiability class, denoted by " \sim " instead of " \approx " (see Section 2 for more details). The variational parameters are denoted by ϕ and φ to match the nomenclature in the rest of the paper.

Figure 1: Variational inference (VI) examples for simulation data x_i and labels z_i indexed by $i = 1 \dots N$, which comprise the whole dataset of size N . The exception is the single event example in (a), which has a single datum x_j as input.

discussed on a per-event level or in the context of neural networks as approximating the posterior over the network parameters in Bayesian neural networks [11]. However, one is really interested in the posterior over physics parameters, ideally for all events simultaneously. Figure 1 b) illustrates that supervised learning, extended supervised learning and unsupervised VAEs can be interpreted as stochastic variational inference using the KL-divergence of the joint distribution of data, observed and unobserved labels (latent variables). Because only sub-parts of the joint distribution are effectively parametrized in these approaches, one obtains "explicit" variational inference solutions for the posterior distributions, in the sense that the conditional structure of the posterior is explicitly modeled and thereby different for each datapoint. This is sometimes also called "local" variational inference [21] in the literature. The unified viewpoint in combination with amortized conditional normalizing flows naturally leads to answers to the following questions:

1. How can we do coverage tests with neural networks on complex base distributions, including distributions over directions?
2. How are systematic uncertainties incorporated in the training process?
3. How can we do goodness-of-fit checks on neural-network predictions?

The first half of the paper is concerned with the unified viewpoint and derives the various loss functions from the joint KL-divergence. The second half then answers the three questions above.

2 Monte Carlo estimates and the joint KL-divergence

Physics experiments perform measurements on the final outcomes of a causal chain of events. These measurements are inherently probabilistic due to the uncertainty principle in quantum mechanics and the measured observable follows a specific probability distribution. The probability distribution over possible measurement outcomes is called the likelihood function when viewed as a function of its parameters. It is a central object in both Frequentist and Bayesian statistical analyses to perform parameter estimation [6]. Its shape

is entirely determined by the laws of nature in combination with the detector response. However, because the laws can be convoluted and the experiment can be very complex, it is usually not possible to write down an explicit analytic expression. A common practice is to estimate the likelihood function from Monte Carlo simulations where all these complex effects are considered [22]. This estimated likelihood function is then used to perform inference or calculate confidence intervals.

Neural networks allow to skip this estimation step completely, because the Monte Carlo samples themselves are not only drawn from the true likelihood function, but more generally from the true joint distribution $\mathcal{P}_t(x, z_o)$ of observations x and parameters of interest z_o . Let us call the corresponding true likelihood function $\mathcal{L}_t(z_o; x) = \mathcal{P}_t(x; z_o)$ where $\mathcal{P}_t(x; z_o)$ is the true probability distribution of the measured data x given the properties z_o . Here z_o stands for *observed* properties in the simulation, for example the position of a particle interaction. Connected to this likelihood function, there exists a true posterior distribution $\mathcal{P}_t(z_o; x)$ and a true prior distribution $\mathcal{P}_t(z_o)$. The true joint distribution follows the distribution which includes the detector response and selection effects inherent to the measurement - it also includes artificial selection effects. For example, if the generating function of the direction of injected particles is uniform, the actually recorded Monte Carlo events will generally not be uniform due to detector effects. The implicitly contained true prior $\mathcal{P}_t(z_o)$ is this non-uniform distribution over z_o of the actually registered events, not the uniform generating distribution.

Since a Monte Carlo simulation draws samples $x_i, z_{o,i}$ from the joint distribution $\mathcal{P}_t(x, z_o)$, we can always evaluate any expectation value under the true joint probability distribution as

$$E_{x, z_o}[f(x, z_o)] = \int_{x, z_o} \mathcal{P}_t(x, z_o) f(x, z_o) dx dz_o \approx \frac{1}{N} \sum_{x_i, z_{o,i}} f(x_i, z_{o,i}) \quad (1)$$

where i indexes the N samples. The following sections make use of a specific choice for f , namely $f = \ln \frac{\mathcal{P}_t(x, z_o)}{q(x, z_o)}$, which yields an expectation value that equals the KL-divergence between two distributions $\mathcal{P}_t(x, z_o)$ and $q(x, z_o)$. The KL-divergence [18] is a natural quantity to measure the distance between two probability distributions. In particular, if q_ϕ is a parametrized probability distribution, the KL-divergence defines a loss function over ϕ that achieves its minimum when q_ϕ is equal to \mathcal{P}_t . It is therefore often used in *variational* methods which perform inference via optimization [21]. It turns out that the joint KL-divergence can be used to derive the loss functions in both supervised learning and unsupervised VAEs and thereby unifies them as two connected approaches to variational inference in slightly different circumstances.

2.1 Supervised learning

The KL-divergence of the true joint distribution $\mathcal{P}_t(z_o, x)$ and an approximation $q_\phi(z_o, x)$ can be written as

$$D_{\text{KL, joint}(x, z_o)}(\mathcal{P}_t; q_\phi) = \int_x \int_{z_o} \mathcal{P}_t(z_o, x) \cdot \ln \frac{\mathcal{P}_t(z_o, x)}{q_\phi(z_o, x)} dz_o dx = \int_x \int_{z_o} \mathcal{P}_t(z_o; x) \cdot \mathcal{P}_t(x) \cdot \ln \frac{\mathcal{P}_t(z_o; x) \cdot \mathcal{P}_t(x)}{q_\phi(z_o; x) \cdot q(x)} dz_o dx \quad (2)$$

$$= \int_x \int_{z_o} \mathcal{P}_t(z_o; x) \cdot \mathcal{P}_t(x) \cdot \left(\ln \frac{\mathcal{P}_t(z_o; x)}{q_\phi(z_o; x)} + \ln \frac{\mathcal{P}_t(x)}{q(x)} \right) dz_o dx \quad (3)$$

$$= \int_x \int_{z_o} \mathcal{P}_t(x) \cdot \mathcal{P}_t(z_o; x) \cdot \ln \frac{\mathcal{P}_t(z_o; x)}{q_\phi(z_o; x)} dz_o dx + \int_x \mathcal{P}_t(x) \cdot \ln \frac{\mathcal{P}_t(x)}{q(x)} dx \quad (4)$$

$$= E_x [D_{\text{KL}}(\mathcal{P}_t(z_o; x); q_\phi(z_o; x))] + D_{\text{KL}}(\mathcal{P}_t(x); q(x)) \quad (5)$$

The distributions involving \mathcal{P}_t can not be evaluated analytically, but as discussed above Monte Carlo simulations yield samples from \mathcal{P}_t and hence provide sample based estimates of the integrals. We only parametrize the conditional distribution over labels, $q_\phi(z_o; x)$ with ϕ , and leave the distribution $q(x)$ unparametrized as it is typically not of interest. Taking the sample estimate yields the following update rule over ϕ to minimize the KL-divergence objective and thereby minimize the supervised loss function $\mathcal{L}_{\text{supervised}}(\phi)$:

$$\arg \min_{\phi} \hat{D}_{\text{KL, joint}(x, z_o)}(\mathcal{P}_t; q_\phi) = \arg \min_{\phi} \frac{1}{N} \sum_{x_i, z_{o,i}} \ln \left(\frac{\mathcal{P}_t(z_{o,i}; x_i)}{q_\phi(z_{o,i}; x_i)} \right) + \ln \left(\frac{\mathcal{P}_t(x_i)}{q(x_i)} \right) \quad (6)$$

$$= \arg \min_{\phi} \frac{1}{N} \sum_{x_i, z_{o,i}} -\ln (q_\phi(z_{o,i}; x_i)) + \text{const} \quad (7)$$

$$= \arg \min_{\phi} \frac{1}{N} \sum_{x_i, z_{o,i}} -\ln (q_\phi(z_{o,i}; x_i)) \quad (8)$$

$$\equiv \arg \min_{\phi} \mathcal{L}_{\text{supervised}}(\phi) \quad (9)$$

The approximation of the marginal likelihood, $q(x_i)$, can be dropped as a constant part with respect to changes in ϕ . Additionally we can drop the true posterior evaluations $\mathcal{P}_t(z_{o,i}; x_i)$ which are also constant with respect to ϕ . If the distribution q_ϕ is actually parametrized by a network whose parameters are ϕ , the derivation shows that minimizing the KL-divergence between the true posterior and an approximation given by a neural network is equivalent to standard neural network training where the goal is to minimize negative log-probability over labels. This has been discussed previously [19], but it is usually described as a maximum likelihood objective with respect to the network parameters. Here, we emphasize that it is really more useful to think of $q_\phi(z_o; x_i)$ as a parametrized posterior over labels z_o given the data x_i , not as a conditional likelihood function with respect to the parameters ϕ . In unsupervised learning the labels $z_{o,i}$ are not available so the precise above objective does not work. In the following we show that a simple replacement of the posterior KL-divergence in eq. 5 with the respective reverse KL-divergence leads to a tractable solution via the reparametrization trick [23] which contains the evidence lower bound (ELBO) and thereby the VAE objective.

2.2 Unsupervised learning: Variational autoencoders

The following derivation is motivated by an experimental physicists' point of view when there is access to a Monte Carlo simulation. Here, one way to think of latent variables in unsupervised variational autoencoders is to imagine them as unobserved labels that are not recorded in the simulation. The implied direct comparison, and renaming, of "observed" into "unobserved" labels is justified if the latent variables have positive mutual information with the data. Mutual information is a non-linear generalization of correlation [24]. In events of a static particle physics detector with a single particle interaction, for example, the only properties that can have positive mutual information with the data are properties of the particle interaction. These properties can be in principle be labeled. Typical labels are the position or direction of a particle at the interaction point.¹

The aim of the following exercise is to start with the same KL-divergence as for the supervised loss, but with unobserved labels z_u instead of observed labels z_o , and deduce which modifications have to be made in order to obtain the ELBO loss of a variational autoencoder as a partial tractable objective. It is not the aim to deduce strict new numerical results, but to indicate how supervised learning and unsupervised learning are precisely connected in the variational viewpoint.

Starting with the same joint KL-divergence, but now using unobserved labels z_u , we can write

$$D_{\text{KL, joint}(x, z_u)}(\mathcal{P}_t; q_\phi) = E_x \left[\int_{z_u} \mathcal{P}_t(z_u; x) \cdot \ln \frac{\mathcal{P}_t(z_u; x) \cdot \mathcal{P}_t(x)}{q_\phi(z_u; x) \cdot q(x)} dz_u \right] \quad (10)$$

$$= E_x [D_{\text{KL}}(\mathcal{P}_t(z_u; x); q_\phi(z_u; x))] + \underbrace{D_{\text{KL, Marg}(x)}(\mathcal{P}_t(x); q(x))}_{\equiv D_{\text{KL, M, const}}} \quad (11)$$

which results in two intractable terms. The second term $D_{\text{KL, M, const}}$ can for further discussion be ignored since $q(x)$ is typically not parametrized and therefore irrelevant in optimization schemes. In the first term, the outer integral over x is explicitly kept, because we do have samples from x and so we can in principle evaluate expectation values over x . The inner part, however, involves an expectation over the intractable KL-divergence of the conditional distribution $\mathcal{P}_t(z_u; x)$ with $q_\phi(z_u; x)$ (orange). In order to proceed to some extent, we could replace the KL-divergence within the expectation value with any generalized divergence measure $\mathcal{D}(\mathcal{P}_t; q)$, for example f-divergences [25], as long as it shares the property that it has a minimum when $\mathcal{P}_t(z_u; x) = q_\phi(z_u; x)$. However, there is only a subset that will straightforwardly lead to the ELBO loss of the VAE. Among those, the natural choice is the reverse KL-divergence, $D_{\text{rev.KL}}(q_\phi(z_u; x); \mathcal{P}_t(z_u; x))$, which we choose for simplicity. This leads to the following surrogate loss term:

$$\text{Surrogate}_{\text{KL}}(\mathcal{P}_t; q_\phi) = E_x [D_{\text{rev.KL}}(q_\phi(z_u; x); \mathcal{P}_t(z_u; x))] + \underbrace{D_{\text{KL, Marg}(x)}(\mathcal{P}_t(x); q(x))}_{\equiv D_{\text{KL, M, const}}} \quad (12)$$

As long as q_ϕ has arbitrary approximation capabilities, the surrogate term has the property that the minimum over the parameters ϕ is equal to the minimum of the original KL-divergence

$$\arg \min_{\phi} D_{\text{KL, joint}(x, z_o)}(\mathcal{P}_t; q_\phi) = \arg \min_{\phi} \text{Surrogate}_{\text{KL}}(\mathcal{P}_t; q_\phi) \quad (13)$$

because both KL-divergence (orange) and reverse KL-divergence (blue) are equal to zero when the two involved distributions are equal. So far this is just a theoretical exercise, as \mathcal{P}_t is inaccessible. The surrogate loss, however, contains the ELBO loss. In order to see this, we can rewrite the surrogate loss as

$$\text{Surrogate}_{\text{KL}}(\mathcal{P}_t; q_\phi) = E_x [D_{\text{rev.KL}}(q_\phi(z_u; x); \mathcal{P}_t(z_u; x))] + D_{\text{KL, M}} \quad (14)$$

¹If the number of latent variables is very large, some of them will be superfluous and not carry any information about the data. For such variables this identification strictly makes no sense since they could never be labeled.

$$= E_x \left[\int_{z_u} q_\phi(z_u; x) \cdot \ln \frac{q_\phi(z_u; x)}{\mathcal{P}_t(z_u; x)} dz_u \right] + D_{\text{KL},M} \quad (15)$$

$$= E_x \underbrace{\left[\int_{z_u} q_\phi(z_u; x) \cdot \ln q_\phi(z_u; x) dz_u \right]}_{\text{entropy term}} + E_x \left[\int_{z_u} q_\phi(z_u; x) \cdot \ln \frac{\mathcal{P}_t(x)}{\mathcal{P}_t(x, z_u)} dz_u \right] + D_{\text{KL},M} \quad (16)$$

$$= E_x \underbrace{\left[\int_{z_u} q_\phi(z_u; x) \cdot \ln \frac{q_\phi(z_u; x) \cdot \mathcal{P}_t(x)}{p_\theta(x; z_u) \cdot p_\psi(z_u)} dz_u \right]}_{D_{\text{KL}}(\mathcal{P}_t(x) \cdot q_\phi(z_u; x), p_{\theta/\psi}(x, z_u))} + E_x \underbrace{\left[\int_{z_u} q_\phi(z_u; x) \cdot \ln \frac{p_\theta(x; z_u) \cdot p_\psi(z_u)}{\mathcal{P}_t(x, z_u)} dz_u \right]}_{\equiv \mathcal{R}(\phi, \theta, \psi)} + D_{\text{KL},M} \quad (17)$$

$$= E_x [\ln \mathcal{P}_t(x)] - E_x \underbrace{\left[\int_{z_u} q_\phi(z_u; x) \cdot \left[\ln p_\theta(x; z_u) - \ln \frac{q_\phi(z_u; x)}{p_\psi(z_u)} \right] dz_u \right]}_{\text{evidence lower bound (ELBO)}} + \mathcal{R}(\phi, \theta, \psi) + D_{\text{KL},M} \quad (18)$$

which results in the negative ELBO loss, two constant terms, and a residual term $\mathcal{R}(\phi, \theta, \psi)$.

The important step in this reformulation is the introduction of an auxiliary distribution $p_{\theta/\psi}(z_u, x) = p_\theta(x; z_u) \cdot p_\psi(z_u)$ from eq. 16 to eq. 17. The entropy term in eq. 16 by itself is tractable, but behaves divergent when optimized over ϕ , so the introduction of $p_{\theta/\psi}(z_u, x)$ is a necessary ingredient to obtain anything that has a chance for non-trivial behavior. We also indicate by the subscript ψ that the prior $p_\psi(z_u)$ can be parametrized by ψ , even though in many applications it is just taken to be a fixed standard normal distribution. With the introduction of $p_{\theta/\psi}(x, z_u)$, the surrogate KL-divergence then splits into two terms in eq. 17.

The first term is the KL-divergence between $\mathcal{P}_t(x) \cdot q(z_u; x)$ and $p_{\theta/\psi}(x, z_u)$, which is equal to the ELBO loss when the constant term $E_x[\ln \mathcal{P}_t(x)]$ is pulled out of the integral. This joint KL-divergence between $\mathcal{P}_t(x) \cdot q_\phi(z_u; x)$ and $p_{\theta/\psi}(x, z_u)$ has been used before in the context of the InfoVAE [26] or more general VAE architectures with additional constraints [27] and is by itself another non-standard starting point to derive the ELBO loss. Here it arises as a product in the derivation which is connected to the supervised loss derivation via the KL-divergence of the joint distribution. It is important to note that we have to use this more complicated construction, compared to just start with this simpler KL divergence, in order to see the similarity to the supervised loss derivation and then be equipped with a canonical way to derive the extended supervised case in Section 2.3.

The second term is a residual term $\mathcal{R}(\phi, \theta, \psi)$. This term is not tractable, because any samples drawn from $q_\phi(z_u; x)$ can not be evaluated by the inaccessible density $\mathcal{P}_t(z_u; x)$. However, one can deduce that after an ELBO optimization with solution θ^* and ϕ^* and flexible enough density parametrizations, the residual term is always bounded from below by zero because it is equal to a proper KL-divergence.

$$q_{\phi^*}(z_u; x) \cdot \mathcal{P}_t(x) \approx p_{\theta^*/\psi^*}(x, z_u) \rightarrow \mathcal{R}(\phi^*, \theta^*, \psi^*) \approx D_{\text{KL}}(q_{\phi^*}(z_u; x) \cdot \mathcal{P}_t(x), \mathcal{P}_t(z_u, x)) \geq 0 \quad (19)$$

This construction therefore makes it explicit that ELBO optimization alone does not necessarily lead to a joint density that matches the true density because \mathcal{R} can be greater than zero - a fact that is lost in the standard ELBO derivation [28] based on the marginal likelihood and Jensen's inequality and therefore also in many papers since the original VAE paper [23]. Furthermore, beside the assumption that we could in principle observe the latent variables but choose not to, hence the term "unobserved", in general we do not know the exact values. Because of the symmetry of the KL-divergence under diffeomorphisms, this allows for extra functional freedom of the distributions and the involved mapping.

Instead of complete freedom, however, it was pointed out in [29] that the determined final distribution matches the true one up to certain class of transformations \mathcal{A} , which they call "identifiability" up to \mathcal{A} . In particular, when all terms in the ELBO depend on extra observed input, the prior has a certain structure and the data x are Gaussian observations, \mathcal{A} turns out to be a global scaling and permutation of latent dimensions.² Regarding the above derivation we can write $\mathcal{R}(\phi^*, \theta^*, \psi^*) \underset{\mathcal{A}}{\sim} 0$ to denote this situation, which means the residual term is zero within the identifiability class \mathcal{A} . Extra constraints on the mutual information between data and labels [26], the total correlation of latent variables [30], a better prior parametrization [31] or extra conditional dependencies [29] are often used to improve the ELBO solution. From the above derivation these are all well motivated, as all of those use extra constraints besides the ELBO and therefore have the potential to reduce $\mathcal{R}(\phi^*, \theta^*, \psi^*)$ within a given identifiability class \mathcal{A} whose properties will depend on the constraints.

²And potentially a further linear transformation, see [29] for details.

We can further form the sample approximation of the ELBO, including extra constraints via $C(\theta, \phi, \psi)$, to form a loss function

$$\arg \min_{\theta, \phi, \psi} \mathcal{L}_{\text{VAE}}(\theta, \phi, \Psi) \equiv \arg \min_{\theta, \phi, \psi} -\widehat{\text{ELBO}}(\theta, \phi, \psi) \left[+ C(\theta, \phi, \psi) / \text{s.t. } C(\theta, \phi, \psi) = 0 \right] \quad (20)$$

$$= \arg \min_{\theta, \phi, \psi} \frac{1}{N} \sum_{x_i, z_{u,i}, \phi} -\ln p_{\theta}(x_i; z_{u,i}, \phi) + \ln \left(\frac{q_{\phi}(z_{u,i}, \phi; x_i)}{p_{\psi}(z_{u,i}, \phi)} \right) \left[+ C(\theta, \phi, \psi) / \text{s.t. } C(\theta, \phi, \psi) = 0 \right] \quad (21)$$

where the brackets indicate that the term $C(\theta, \phi, \psi)$ can either be an extra term in the loss function or it directly describes a constraint equation. As discussed before, if flexible enough density estimators are used and the final parameter solution is denoted by θ^* , ϕ^* and ψ^* , it follows that $\mathcal{R}(\phi^*, \theta^*, \psi^*) \underset{\mathcal{A}}{\sim} 0$, the ELBO saturates, and $\text{Surrogate}_{\text{KL}}(\mathcal{P}_t; q_{\phi^*}) \underset{\mathcal{A}}{\sim} 0$ and $D_{\text{KL}, \text{joint}(x, z_o)}(\mathcal{P}_t; q_{\phi^*}) \underset{\mathcal{A}}{\sim} 0$.

In our view, a few advantages arise from this derivation of the variational autoencoder.

1. The derivation is connected to the KL-divergence derivation of supervised learning.
2. It explicitly shows that there are three joint distributions involved. The first is $\mathcal{P}_t(z_u; x) \cdot \mathcal{P}_t(x)$, the true underlying joint distribution. The second is $q_{\phi}(z_u; x) \cdot \mathcal{P}_t(x)$, a distribution where the conditional distribution over the latent variables is exchanged for a tractable approximation $q_{\phi}(z_u; x)$. The third is another tractable approximation $p_{\theta}(x; z_u) \cdot p_{\psi}(z_u)$ which is parametrized in the opposite causal direction. In the literature, the true distribution \mathcal{P}_t is typically simply denoted by p , going back to the original ELBO marginal likelihood derivation [28] or VAE publication [23]. This can be confusing, as p (i.e. \mathcal{P}_t) and p_{θ} are often used interchangeably.
3. Extra constraints [27] [29] [32] are often invoked in practical VAE training to find a better solution than in vanilla VAE training, but this is not well-motivated in the original VAE derivation. The residual term \mathcal{R} explicitly shows why this practice is useful. It is desired to try to reduce \mathcal{R} , and thereby $D_{\text{KL}}(q_{\phi^*}(z_u; x) \cdot \mathcal{P}_t(x), \mathcal{P}_t(z_u, x))$, within a given identifiability class \mathcal{A} by invoking extra constraints on top of the ELBO loss.
4. Because of the connection to the supervised loss, there is a natural path to derive the extended supervised loss as discussed in the next section. This is the most important aspect of this construction for practical applications, because the extended supervised loss allows to calculate a goodness-of-fit (see Section 7).

2.3 Extended supervised and semi-supervised learning

Now let us assume that we have a fixed number of observed and unobserved latent variables z_o and z_u , respectively. The KL-divergence of the joint distribution can then be expanded as

$$D_{\text{KL}, \text{joint}(x, z_o, z_u)}(\mathcal{P}_t; q) \quad (22)$$

$$= \int_x \int_{z_o} \int_{z_u} \mathcal{P}_t(z_u, z_o, x) \cdot \ln \frac{\mathcal{P}_t(z_u, z_o, x)}{q(z_u, z_o, x)} dz_u dz_o dx \quad (23)$$

$$= E_x \left[\int_{z_o} \mathcal{P}_t(z_o; x) \underbrace{\int_{z_u} \mathcal{P}_t(z_u; z_o, x) \ln \frac{\mathcal{P}_t(z_u; z_o, x)}{q_{\phi}(z_u; z_o, x)} dz_u}_{\equiv D_{\text{KL}}(\mathcal{P}_t(z_u; z_o, x); q_{\phi}(z_u; z_o, x))} dz_o \right] + \underbrace{E_{x, z_o} \left[\ln \frac{\mathcal{P}_t(z_o; x)}{q_{\phi}(z_o; x)} \right] + E_x \left[\ln \frac{\mathcal{P}_t(x)}{q(x)} \right]}_{\equiv \mathcal{S}(\varphi)} \quad (24)$$

where the first term involves an intractable KL-divergence similar to the VAE and the second term is the supervised loss function which we abbreviate by \mathcal{S} . Next we construct a surrogate term similar to the VAE derivation in order to obtain a tractable objective.

$$\text{Surrogate}_{\text{KL},1} = E_x \left[\int_{z_o} \mathcal{P}_t(z_o; x) \int_{z_u} q_{\phi}(z_u; z_o, x) \ln \frac{q_{\phi}(z_u; z_o, x)}{\mathcal{P}_t(z_u; z_o, x)} dz_u dz_o \right] + \mathcal{S}(\varphi) \quad (25)$$

In this term we again replace the KL-divergence (orange) by a reverse KL-divergence (blue). In contrast to the VAE, we can define a second surrogate term as

$$\text{Surrogate}_{\text{KL},2} = E_x \left[\int_{z_o} \tilde{q}_{\phi}(z_o; x) \int_{z_u} q_{\phi}(z_u; z_o, x) \ln \frac{q_{\phi}(z_u; z_o, x)}{\mathcal{P}_t(z_u; z_o, x)} dz_u dz_o \right] + \mathcal{S}(\varphi) \quad (26)$$

where the expectation is taken with respect to the parametrized distribution $\tilde{q}_\varphi(z_o; x)$ (turquoise) that is determined in the supervised part \mathcal{S} . The tilde indicates that gradients with respect to φ are not propagated through, which is used to completely decouple the supervised from the unsupervised part during learning. This second surrogate loss will be useful for consistent goodness-of-fit procedures (Section 7). If flexible enough density estimators are used, we can observe that

$$\arg \min_{\phi, \varphi} D_{\text{KL}, \text{joint}(x, z_u, z_o)}(\mathcal{P}_t; q_{\phi/\varphi}) = \arg \min_{\phi, \varphi} \text{Surrogate}_{\text{KL}, 1}(\phi, \varphi) \quad (27)$$

$$= \arg \min_{\phi, \varphi} \text{Surrogate}_{\text{KL}, 2}(\phi, \varphi) \quad (28)$$

since the supervised part leads to $\tilde{q}_\varphi(z_o; x) \approx \mathcal{P}_t(z_o; x)$ and the surrogate losses have the same global minimum as the joint KL-divergence, similar to the VAE derivation.

Next, we reformulate the second surrogate loss as

$$\text{Surrogate}_{\text{KL}, 2} \quad (29)$$

$$= E_x \left[\int_{z_o} \int_{z_u} \tilde{q}_\varphi(z_o; x) \cdot q_\phi(z_u; z_o, x) \cdot \ln \frac{q_\phi(z_u; z_o, x)}{\mathcal{P}_t(z_u; z_o, x)} dz_u dz_o \right] + \mathcal{S}(\varphi) \quad (30)$$

$$= E_x \left[\int_{z_o} \int_{z_u} \tilde{q}_\varphi(z_o; x) \cdot q_\phi(z_u; z_o, x) \cdot \ln \frac{q_\phi(z_u; z_o, x) \cdot \mathcal{P}_t(z_o, x)}{\mathcal{P}_t(z_u, z_o, x)} dz_u dz_o \right] + \mathcal{S}(\varphi) \quad (31)$$

$$= E_x \left[\int_{z_o} \int_{z_u} \tilde{q}_\varphi(z_o; x) \cdot q_\phi(z_u; z_o, x) \ln \frac{q_\phi(z_u; z_o, x) \cdot \mathcal{P}_t(z_o, x)}{p_\theta(x; z_o, z_u) \cdot p_\psi(z_o, z_u)} dz_u dz_o \right] \quad (32)$$

$$+ E_x \left[\int_{z_o} \int_{z_u} \tilde{q}_\varphi(z_o; x) \cdot q_\phi(z_u; z_o, x) \ln \frac{p_\theta(x; z_o, z_u) \cdot p_\psi(z_o, z_u)}{\mathcal{P}_t(x, z_o, z_u)} dz_u dz_o \right] + \mathcal{S}(\varphi) \quad (32)$$

$$\equiv \mathcal{R}(\theta, \phi, \varphi, \psi)$$

$$= E_x \left[\int_{z_o} \tilde{q}_\varphi(z_o; x) \cdot \ln(\mathcal{P}_t(z_o, x)) dz_o \right] + E_x \left[\int_{z_o} \int_{z_u} \tilde{q}_\varphi(z_o; x) \cdot q_\phi(z_u; z_o, x) \ln \frac{q_\phi(z_u; z_o, x)}{p_\theta(x; z_o, z_u) \cdot p_\psi(z_o, z_u)} dz_u dz_o \right] \quad (33)$$

ELBO-like

$$+ \mathcal{R}(\theta, \phi, \varphi, \psi) + \mathcal{S}(\varphi)$$

and we end up with a supervised term \mathcal{S} and similar terms to the unsupervised derivation. The residual term $\mathcal{R}(\theta, \phi, \varphi, \psi)$ again is equal to a KL-divergence up to a certain identifiability class after training. There is a slight difference, in that the prior in the ELBO is now defined over the joint space (z_u, z_o) instead of just z_u alone. The same derivation would work with the first surrogate loss by replacing $\tilde{q}_\varphi(z_o; x)$ with $\mathcal{P}_t(z_o; x)$ everywhere. In particular, if in addition to using the first surrogate loss, the joint prior is split up as $p_\psi(z_o, z_u) = p_\psi(z_u; z_o) \cdot p_\psi(z_o)$, every part of the resulting ELBO objective is conditioned on z_o as an extra parameter. This is an important factor for identifiability guarantees, as outlined in [29], and might be interesting to study on its own. We use the second surrogate loss here to later have self-consistent goodness-of-fit calculations (see Section 7) at all times during training. In the following, we discuss two types of loss functions that can be formed using the previous results.

Extended supervised loss The first is a loss definition that can be used to perform what we call *extended supervised training*, and will be important for the calculation of a goodness-of-fit as described in Section 7. It is a sample based application of the tractable parts in eq. 33: the ELBO, the supervised part.

$$\arg \min_{\theta, \phi, \varphi, \Psi} \mathcal{L}_{\text{ext. supervised}}(\theta, \phi, \varphi, \Psi) \quad (34)$$

$$= \arg \min_{\theta, \phi, \varphi, \Psi} \frac{1}{N} \sum_{x_i, \tilde{z}_{o, i, \varphi}, z_{u, i, \phi}} \ln(\mathcal{P}_t(\tilde{z}_{o, i, \varphi}, x_i)) + \ln \frac{q_\phi(z_{u, i, \phi}; \tilde{z}_{o, i, \varphi}, x_i)}{p_\theta(x_i; \tilde{z}_{o, i, \varphi}, z_{u, i, \phi}) \cdot p_\Psi(\tilde{z}_{o, i, \varphi}, z_{u, i, \phi})} + \hat{\mathcal{S}}(\varphi) \quad (35)$$

$$+ \left[C(\theta, \phi, \varphi, \psi) / \text{s.t. } C(\theta, \phi, \varphi, \psi) = 0 \right]$$

$$= \arg \min_{\theta, \phi, \varphi, \Psi} \frac{1}{N} \sum_{x_i, \tilde{z}_{o, i, \varphi}, z_{u, i, \phi}} \ln \frac{q_\phi(z_{u, i, \phi}; \tilde{z}_{o, i, \varphi}, x_i)}{p_\theta(x_i; \tilde{z}_{o, i, \varphi}, z_{u, i, \phi}) \cdot p_\Psi(\tilde{z}_{o, i, \varphi}, z_{u, i, \phi})} + \underbrace{\frac{1}{N} \sum_{S \in x_i, z_{o, i}} -\ln(q_\varphi(z_{o, i}; x_i))}_{\mathcal{L}_{\text{supervised}}} \quad (36)$$

$$+ \left[C(\theta, \phi, \varphi, \psi) / \text{s.t. } C(\theta, \phi, \varphi, \psi) = 0 \right]$$

We again add a constraint term $C(\theta, \phi, \varphi, \psi)$ similar to the VAE loss to potentially improve the identifiability of the unsupervised dimensions z_u . The true observed labels are denoted by $z_{o,i}$ and samples from $\tilde{q}_\varphi(z_o; x)$ are denoted by $\tilde{z}_{o,i,\varphi}$ where the tilde again denotes the gradient is not propagated to decouple the supervised part during training. If the other surrogate term $\text{Surrogate}_{\text{KL},1}$ (eq. 25) had been used, this decoupling would have happened automatically. Because the supervised training is effectively decoupled, one can also choose to first train the supervised part $\mathcal{L}_{\text{supervised}}$, and only later train the rest. An extended supervised training can therefore always be started with an already finished supervised model and can be viewed as an add-on to it.

Semi-supervised learning The extended supervised loss can also be adapted for semi-supervised learning. In semi-supervised learning, parts of the training data have labels, and parts are unlabeled. In the derivation of the VAE loss we argued that latent variables that share mutual information with the data can in principle be labeled. In semi-supervised learning, this assumption is automatically implied - parts of the data are not labeled, but could be in principle. Taking the variational viewpoint of the previous sections, a naive solution might be to use the supervised loss for data with labels, the VAE-loss for data without labels, and use the same distribution q_ϕ in both losses to share parameters. A more natural solution, however, is to use the extended supervised loss instead of the pure supervised loss.

$$\arg \min_{\theta, \phi, \varphi, \Psi} \mathcal{L}_{\text{semi-supervised}}(\theta, \phi, \varphi, \Psi) \quad (37)$$

$$= \arg \min_{\theta, \phi, \varphi, \Psi} \begin{cases} \mathcal{L}_{\text{ext.supervised}}(\theta, \phi, \varphi, \Psi) & \text{(labeled data)} \\ \mathcal{L}_{\text{VAE}}(\theta, \phi, \varphi, \Psi) & \text{(unlabeled data)} \end{cases} \quad (38)$$

For unlabeled data, we take the loss of the variational autoencoder over the combined space $z_{\text{comb}} = \{z_o, z_u\}$ and treat the combined variable as unsupervised. Because the parametrization does not change for data with or without labels, only the sampling strategy differs, this Ansatz seems to be an elegant and natural way to unify both types of data.

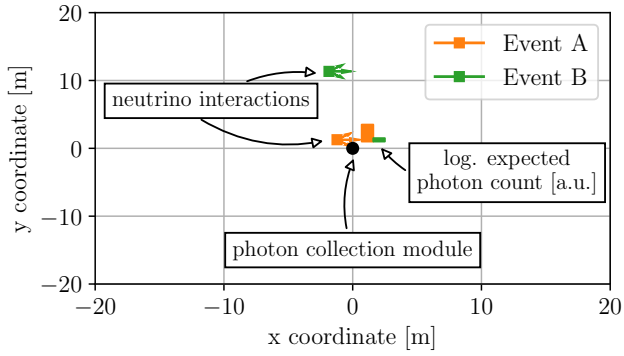
3 Toy Monte Carlo

Several toy Monte Carlo datasets have been created to perform empirical tests in the following sections. They are designed to mimic electromagnetic showers of electron-neutrino interactions [33] in a Cherenkov neutrino detector like IceCube [8] in a 2-D setting. In reality, such showers consist of charged particles that emit Cherenkov light in a coherent light front at the Cherenkov angle that changes its shape as detection modules are further away from the interaction point [34]. For ice, which is the detection medium in IceCube, the light front becomes nearly isotropic for large distances. In general, depending on the position and orientation of the shower with respect to a detection module, the shape of the resulting arrival time distribution of photons varies. In this toy simulation the arrival time distribution is parametrized by a gamma distribution. In addition, the expected number of detected photons falls off exponentially with distance and depends on the orientation of the shower with respect to the module. These PDFs are parametrized such that they qualitatively mimic the photon PDF behavior of the real IceCube detector[8]. At detection, the actual number of observed photons follows a Poisson distribution. Fig. 2 illustrates the first two datasets that are used in the next sections.

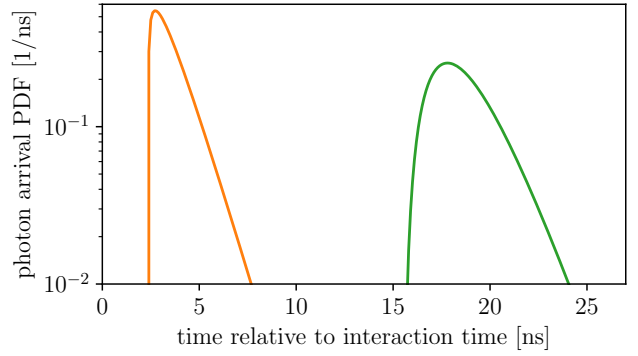
Fig. 2 (a) shows a detector that consists of a single module with two example neutrinos A and B . The two bars next to the photon collection module indicate the logarithmic expected mean of the number of observed photons from each neutrino interaction. Fig. 2 (b) shows the two corresponding photon arrival distributions. For event A , the data distribution is more concentrated than for event B , because the particle interacts closer to the detection unit. Also the number of observed photons is larger. Fig. 2 (c) shows the configuration of a second set of Monte Carlo simulations for a larger detector and a simulated threshold condition that at least 5 photons are observed for an event to be recorded. Also depicted are two associated example events (C and D) together with their expected number of photons in the various photon collection modules.

A summary of all datasets is given in table 1. Dataset 1 and 2 have two intrinsic degrees of freedom, the position of each neutrino interaction. The deposited energy and thereby emitted photons is always the same. A third dataset has an additional degree of freedom by also randomizing the direction. Datasets four to six involve a larger detector and four degrees of freedom, by also sampling the energy of events from an E^{-1} falling energy spectrum between 1 and 100 GeV. The last dataset, which contains track-like topologies, effectively emulates relativistic muon tracks by putting multiple electromagnetic showers along a track that moves with the speed of light and distributing the energy in equal parts among those losses. More information on how these more complex datasets are used is given in Section 7 and in appendix A.

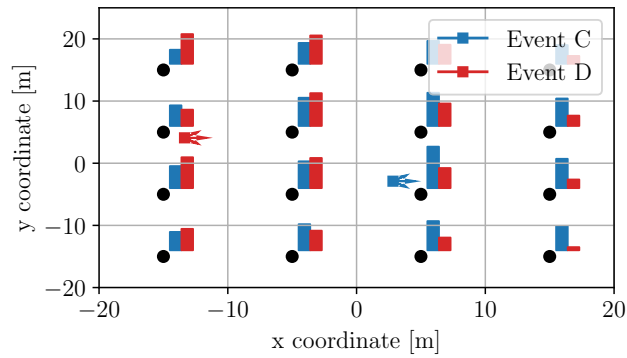
The detection process can be described by an inhomogeneous tempo-spatial Poisson point process [35]. The spatial part is restricted to the position of the collection modules, while the temporal detection can happen at all times. The corresponding likelihood function for observed labels z_o is an extended likelihood



(a)



(b)



(c)

Figure 2: Illustration of the two simplest toy Monte Carlo datasets. Black dots denote collection modules, squares with arrows indicate shower-like neutrino events and vertical bars expected logarithmic photon yield in a given photodetector. (a) Dataset 1 (single photodetector) with two example events A and B. (b) Photon arrival time distributions of events A and B. (c) Dataset 2 (16 photon collectors) with two example events C and D.

	no. modules	d.o.f.	event	other
dataset 1	1	2 (pos.)	shower-like	> 1 obs. photon
dataset 2	16	2 (pos.)	shower-like	> 5 obs. photons
dataset 3	16	3 (pos.+dir.)	shower-like	> 5 obs. photons
dataset 4	400	4 (pos.+dir.+energy)	shower-like	> 5 obs. photons, $ x , y < 55\text{m}$, $E \propto E^{-1}$
dataset 5	400	4 (pos.+dir.+energy)	shower-like	> 5 obs. photons, $E \propto E^{-1}$
dataset 6	400	4 (pos.+dir.+energy)	track-like	> 5 obs. photons, $E \propto E^{-1}$

Table 1: Properties of the datasets used for various comparisons. The detector geometry is always similar to dataset 1 or dataset 2 as depicted in Fig. 2.

[36], which can be written as

$$\mathcal{L}(z_o; \mathbf{k}, \mathbf{t}; z_o) = \mathcal{P}_t(\mathbf{k}, \mathbf{t}; z_o) = \prod_{j=1}^N \frac{\exp^{-\lambda_j(z_o)} \cdot \lambda_j(z_o)^{k_j}}{k_j!} \prod_{i=1}^{k_j} p_j(t_i; z_o) \quad (39)$$

where for a total number of modules N , λ_j is the expectation value of a Poisson distribution for module j , k_j the detected number of photons in module j , and $p_j(t_i)$ the photon arrival probability distribution in module j with observed photon times t_i .

4 The importance of flow-based models

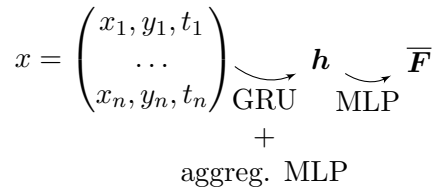
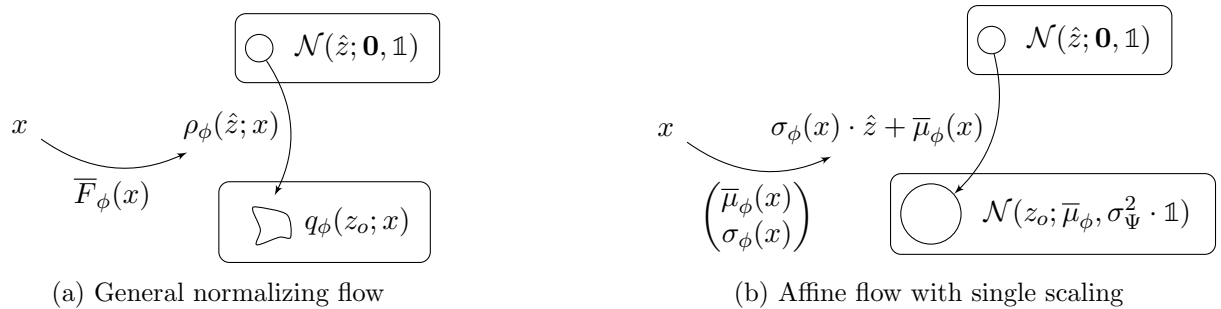
All derivations so far assumed non-specific parametrizations of conditional probability density functions, i.e. posteriors and likelihoods, with neural networks. A general way to parametrize a probability density function with a neural network is via conditional amortized normalizing flows [37] [20]. Normalizing flows are defined using a flow-defining function $\rho(\hat{z})$. This function can be used as $z_o = \rho_\phi(\hat{z})$ to transform a base random variable \hat{z} , in this case following a standard normal distribution, to the desired target random variable z_o . For normalizing flows to work, this function has to be invertible and differentiable, i.e. it has to be a diffeomorphic. If these properties are satisfied, then denoting the probability density of the base by $p_b(\hat{z})$ and the target by $q(z_o)$ we can calculate the log-probability of the target

$$\ln(q(z_o)) = \ln(p_b(\rho_\phi^{-1}(z_o))) - \ln(\det(J_{\hat{z}}^{\rho_\phi})) \quad (40)$$

where $J_{\hat{z}}^{\rho_\phi}$ is the Jacobian of ρ_ϕ with respect to \hat{z} . Flows can be composed of multiple other flows $\rho = \rho_1 \circ \rho_2 \cdots \circ \rho_n$ and the resulting log-probability simply involves a sum over all log-determinants. In general $p_b(\hat{z})$ can be arbitrary, but for simplicity and the possibility to calculate coverage (see Section 6) we use the standard normal distribution. One can also generate samples from $q(z_o)$ by first sampling \hat{z}_i from $p_b(\hat{z})$ and then transform the samples via $z_{o,i,\phi} = \rho_\phi(\hat{z}_i)$, where the samples now depend on the network parameters ϕ . This makes the samples differentiable, known as the reparametrization trick [23], and is a key feature in the variational autoencoder and extended supervised losses (Section 2.3).

Standard normalizing flows only describe PDFs without conditional dependencies, but we would like them to describe conditional PDFs like the posterior distribution. A natural way to make the resulting probability distribution conditional on x , i.e. describe $q(z_o; x)$, is to make the transformation ρ dependent on x via non-linear transformation, as indicated in Fig. 3 (a). In general, a neural network that takes x as an input predicts the parameters \bar{F} , which in turn defines $\rho_\phi(\hat{z}; x) = \rho(\hat{z}; \bar{F}_\phi(x))$. As a specific example, Fig. 3 (b) shows an affine flow where a neural network predicts a mean vector $\bar{\mu}$ and a width σ when the base distribution is a standard normal distribution. The resulting probability distribution $q_\phi(z_o; x)$ of this flow describes a symmetric Gaussian distribution with mean $\bar{\mu}$ and standard deviation σ . This is a common choice in some regression problems in high-energy neutrino physics [38] and used later in some comparisons. The most common choice in supervised learning is to fix $\sigma = 1$, which results in a Gaussian PDF with unit variance which corresponds to the Mean-Squared-Error (MSE) loss function. Generic conditional normalizing flows with a standard normal distribution as base distribution therefore naturally generalize the MSE-loss. In order to describe distributions that are defined simultaneously over the direction and position of an interaction, we can define the normalizing flow over a product space of manifolds. In the example of a 2-dimensional position and 1-dimensional direction, which appears in the toy simulation in Section 3, this space would be $\mathcal{R}^2 \times \mathbb{S}^1$, i.e. 2-dimensional Euclidean space and a 1-sphere. We use an autoregressive structure similar to [39] to connect the PDFs over the different manifolds and create a joint PDF on the tensor product space. In order to still use a combined 3-dimensional Gaussian base distribution, we employ some transformations from the plane to the sphere as described in Section 6. As we discuss there, this allows to calculate coverage for such tensor product distributions.

In all further comparisons, we split the parameters of flow-based posteriors into two parts. The first part consists of an encoder with gated recurrent units (GRUs) [40] and a subsequent aggregate MLP to encode

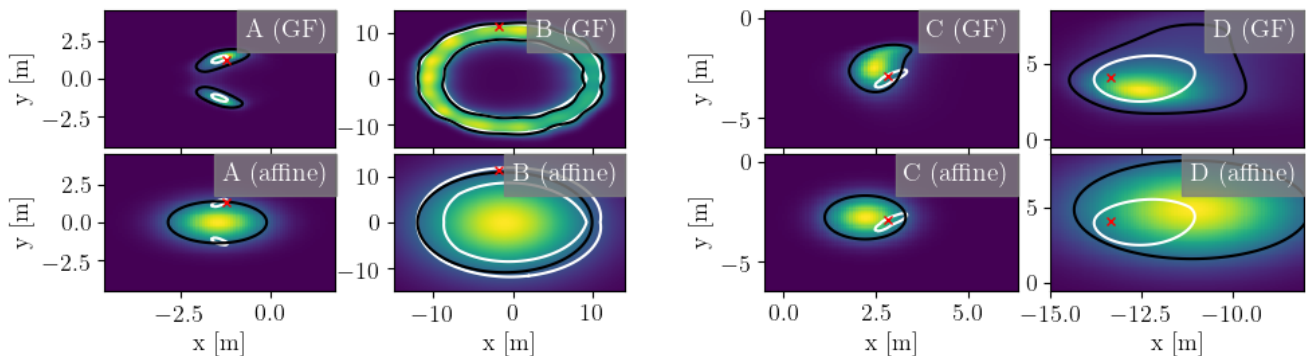


(c) Common data encoding for all experiments.

Figure 3: General flow (a) and a specific affine flow (b) parametrization of the approximate posterior in supervised learning. Choosing $\sigma_\phi = 1$ yields a shifted standard normal distribution which is the PDF used in the MSE loss. General normalizing flow parameters are denoted by \bar{F} . The common encoding scheme for all experiments is depicted in (c), which amortizes the parameters \bar{F} .

the data into an internal representation \mathbf{h} . The GRU reads in a time-ordered sequence of photons, where each photon is characterized by its detected position and time. The second part is a multi-layer perceptron with 2 layers that further maps that internal representation to the respective flow parameters \bar{F} . The process is illustrated in Fig. 3 (c). At the end of training we adopt stochastic weight averaging (SWA) [41]. We found this to reduce the fluctuations and find a rather stable solution. More details on the architecture and on the training procedure is given in appendix B.

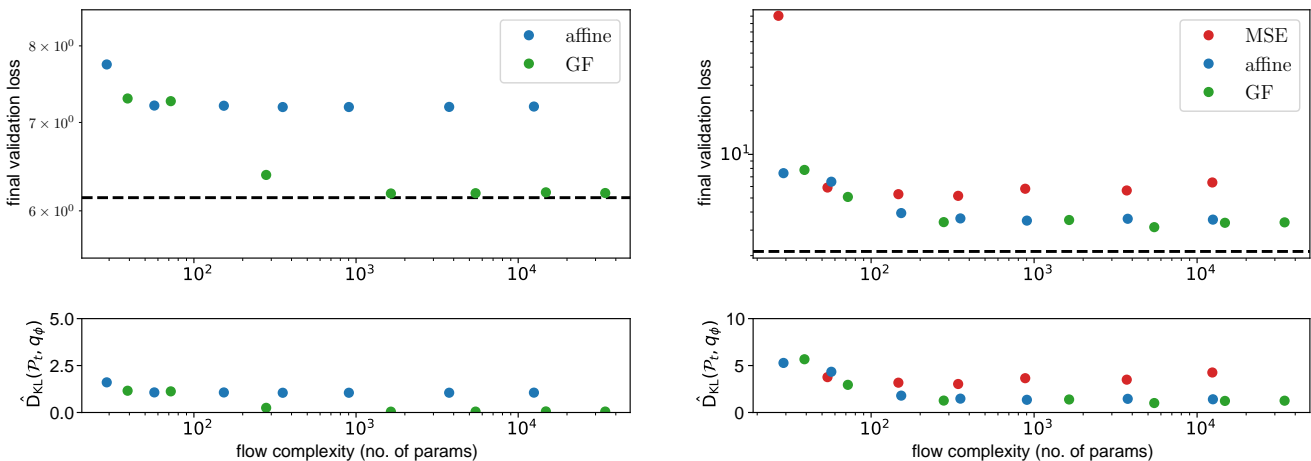
With the likelihood function (eq. 39) and the inherent prior distribution we can construct a true posterior distribution. In the following we assume a flat prior for simplicity. We can then compare the true posterior with the posterior approximations obtained using various normalizing flows after training. Fig. 4 shows such a comparison for the example events from the previous section. It compares a flexible Gaussianization flow [42] with an affine flow (see Fig. 3 for details). For dataset 1, which consists of a single photon collection module, the resulting posterior is highly non-Gaussian. The flexible Gaussianization flow can approximate the posterior much better than an affine flow with a single width parameter. For dataset 2 the events generally contain more observed photons and the posteriors become more Gaussian-like. Both flows have more comparable shapes in this example. To assess performance more generally, Fig. 5 shows the posterior approximation quality versus the number of parameters of the second part of the flow. The number of parameters of the first GRU encoder part is held fixed and not included in the quantity displayed on the x-axis. The second part, which consists of an MLP with two layers, is varied in its hidden dimension. For the Gaussianization flow, additionally the number of flow parameters is varied, which specifically for Gaussianization flows leads to more internal layers and more kernel basis elements (see appendix B for details). In general, the flexible Gaussianization flow is more parameter efficient than the simpler affine flow. As can be seen in Fig. 5 b), the MSE loss with a standard normal posterior is roughly the same scale as the other posterior approximations in dataset 2, and the corresponding KL-divergence to the true posterior only a little worse than for an affine or Gaussianization flow. This happens by chance here, since true posteriors have various shapes and scales and no reason to match a standard normal distribution. For dataset 1 (Fig. 5 a)), on the other hand, the standard normal using the MSE-loss is much worse in terms of KL-divergence to the true posterior and therefore not shown in the figure. The better parameter efficiency of the Gaussianization flow has to do with the possibility to adjust the potential complexity of the flow itself, i.e. increase the size of \bar{F} . For an affine flow, on the other hand, \bar{F} is fixed to be a mean $\bar{\mu}$ and width σ , and one can only increase the complexity by increasing the MLP hidden dimension. In all cases, the final performance saturates, where more parameters do not help performance. The Gaussianization flow should in principle be flexible enough to describe all true posterior shapes in the training dataset, so this saturation is not related to the normalizing flow capabilities. It can be either because more training data is required for this more complex data or the encoding architecture needs to be improved - or a combination of both. We come back to the latter point in the discussion at the very end of the paper.



(a) Posterior scans of dataset 1 example events.

(b) Posterior scans of dataset 2 example events.

Figure 4: A comparison of posteriors of the position for the example events A and B from dataset 1 and events C and D from dataset 2. The normalizing flow posterior is shown together with a 68% contained probability mass in black. The 68% probability mass contour of the true posterior assuming a flat prior is shown in white. The true event positions are marked in red. The upper row shows the result for Gaussianization flows, the lower row for an affine flow (a Gaussian) with a single covariance parameter.



(a) Performance vs. complexity for dataset 1.

(b) Performance vs. complexity for dataset 2.

Figure 5: Posterior approximation performance of a Gaussianization flow [42] (GF), an affine flow with a single variable width σ (affine), and an affine flow with $\sigma = 1$ (MSE). Along the x-axis the number of parameters and the potential flow complexity increases, while the encoding complexity is held fixed (see text). The respective upper plot shows the validation loss. The black dotted line shows the loss obtained from the true posterior. The respective lower plot shows the sample-based KL-divergence.

5 Systematic Uncertainties

A standard practice to incorporate systematics in a both Frequentist and Bayesian analyses is to first assume they can be parametrized by a parameter ν which follows a statistical distribution, for example a Gaussian with a known mean and width, e.g. $p(\nu; \mu_\nu, \sigma_\nu)$. Such a parametrization does not make sense in a Frequentist sense, but should rather be understood subjectively as the ignorance about the true value of the systematic parameter ν in question. In a Frequentist analysis, usually every systematic is then included as a log-probability penalty term in the likelihood function with respective nuisance parameters in a profile likelihood approach [43]. In a Bayesian analysis the systematic uncertainties influence the joint distribution of x and θ , i.e. $p(x, \theta) \rightarrow p(x, \theta; \nu)$. A marginalized joint density can then be obtained as $\mathcal{P}_{t,M}(x, \theta) = \int p(x, \theta; \nu)p(\nu)d\nu$. Because it applies to the joint distribution, it also applies to any term in Bayes' theorem,

$$\mathcal{P}_t(\theta; x, \nu) = \frac{\mathcal{P}_t(x; \theta, \nu)\mathcal{P}_t(\theta; \nu)}{\mathcal{P}_t(x; \nu)} \quad (41)$$

and one can for example obtain the marginalized posterior as

$$\mathcal{P}_{t,M}(\theta; x) = \int \mathcal{P}_t(\theta; x, \nu) \cdot p(\nu)d\nu \quad (42)$$

which now includes the extra uncertainty about the systematics parameter ν .

In the previous sections we discussed how supervised learning and VAEs approximate the underlying distributions of interest via variational inference. A Monte Carlo simulation that first draws systematic parameters ν and then records events with labels θ and data x according to the detector response will automatically produce samples from $\mathcal{P}_{t,M}(\theta, x)$ or any true conditional distribution of interest. These are the distributions that the neural network will approximate. Incorporating systematics is therefore possible at no change of the underlying procedure, as long as the simulation one is using for training additionally samples from the systematic distributions. No explicit form of the PDF of the systematic parameters has to be known, only sampling is required. For supervised learning, for example, one can just replace any term \mathcal{P}_t by $\mathcal{P}_{t,M}$ in eq. 5 and the neural network based approximation q_ϕ will approximate the marginalized true posterior $\mathcal{P}_{t,M}(\theta; x)$. It is already common practice in modern high-energy physics experiments to generate Monte Carlo simulations with potentially marginalized systematic parameters [44], so there is no overhead in actually including those uncertainties. The next section illustrates the coverage behavior of the variational posterior including such marginalization.

6 Coverage of the neural network posterior

In Frequentist or Bayesian analyses it is important to know how well confidence or credible intervals cover the true values. In a Frequentist analysis, in the limit of large amounts of data, Wilks' Theorem [45] implies that the quantity $\lambda = -2 \cdot (\ln L(\theta_t) - \ln L(\theta_0))$ is χ_ν^2 distributed with ν corresponding to the dimensionality of θ when θ_0 is the value that maximizes the likelihood function and θ_t the true value that generated the data. It is connected to the fact that likelihood scans around the optimum have an approximately Gaussian shape in the large-data limit. A similar statement appears in a Bayesian analysis from the Bernstein-von-Mises theorem [46], which implies that for large amounts of data the posterior $p(\theta; x)$ becomes Gaussian. For any n-dimensional multivariate Gaussian the quantity $(x - \mu)C^{-1}(x - \mu)$ is χ_n^2 distributed [47], which again implies the quantity $\lambda_{\text{Bayes}} = -2 \cdot (\ln p(\theta_t; x) - \ln p(\theta_0; x))$ is also χ^2 distributed in the Gaussian limit of $p(\theta; x)$.

Both of these coverage calculations require the assumption of the large-data limit. With normalizing flows that have a Gaussian distribution as base distribution, we can use the same methodology to calculate exact coverage for a target distribution of *any* shape. By construction, samples following a target $q_\phi(z_o)$ are generated by drawing samples \hat{z}_i from a standard-normal base distribution³ $p_b(\hat{z})$ and subsequent application of $\rho(\hat{z})$. We can invert this logic and for any target sample $z_{o,i}$ transform it back to the Gaussian base using the inverse transformation $\hat{z}_i = \rho^{-1}(z_{o,i})$. This is indicated in Fig. 7 a). If the samples $z_{o,i}$ follow the target $q_\phi(z_o)$, the corresponding samples \hat{z}_i at the base must follow a standard normal distribution, and this implies the quantity $\lambda_{\text{base}} = -2 \cdot (\ln p_b(\hat{z}) - \ln p_b(0))$ is again χ^2 distributed. Figure 6 shows that central intervals at the base distribution, which are related to the χ^2 distribution, transform in the target space to connected intervals because of the diffeomorphism connecting the two spaces. The normalizing-flow relation (eq. 40) ensures that the interval still covers the same probability mass. However, the interval in the target space does not have a fixed positioning, like the unique probability mass-ordered interval indicated in the right plot in Fig. 6. For conditional normalizing flows, these intervals also change based on the conditional input. This non-uniqueness of the tested interval is not an issue, since typical coverage curves test many percentages in unison (see Fig. 8), and can still be interpreted similarly: percentage values above the diagonal cover more than expected, percentage values below the diagonal less than expected. These regions can just not be identified with the unique probability mass-ordered interval one would usually have in the Gaussian case.

³For simplicity we use a standard normal in all experiments, but the coverage calculation works for an arbitrary Gaussian base distribution.

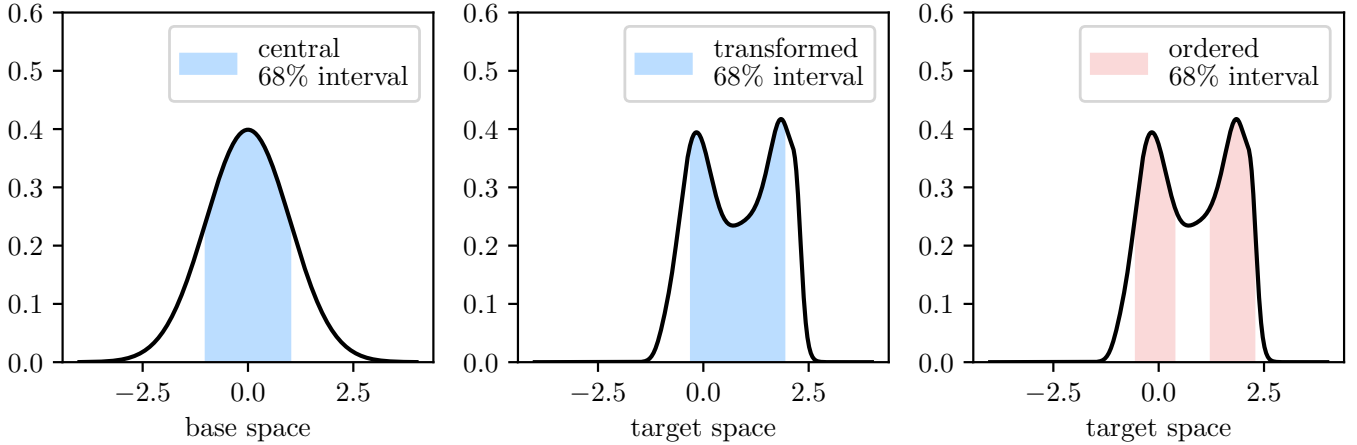


Figure 6: Transformation of the central 68% interval at the base space distribution (left) to the target space distribution (center) for a 1-d normalizing flow with two peaks. The unique probability-mass ordered 68% interval for the target space distribution is shown in the right plot.

We can further extend this coverage calculation to posteriors on manifolds like spheres. In [48] the authors discuss how to define a flexible normalizing flow on a sphere via stereographic projection of a normalizing flow in the plane. A more stable alternative turns out to be directly to start with a base distribution on the sphere and parametrize a flexible flow which is intrinsic to the manifold [49]. We can combine both of these ideas to define a flexible flow on the sphere that also allows to define coverage. The methodology is illustrated in Fig. 7 b) and consists of multiple sub-flows.

The base distribution is again a standard normal distribution in \mathbb{R}^n . It is transformed to another distribution in \mathbb{R}^n that itself corresponds to the flat distribution on the n -sphere once it is stereographically projected. Then follows the stereographic projection, and finally the intrinsic flow on the sphere. The first two flows from the standard normal in \mathbb{R}^n to the flat distribution on the sphere can be combined without actually invoking a Riemannian manifold flow which normally would involve the calculation of the gram matrix $J^T J$ where J would be the Jacobian of the given manifold mapping. To do so, the distributions in the plane are first written in spherical coordinates. The radial coordinate of the Gaussian distribution in \mathbb{R}^n is then transformed to θ_{d-1} on the sphere, while the remaining angular coordinates $(\theta_1, \dots, \theta_{d-2}, \phi)$ stay unchanged. The end result of these transformations turns out to be (see appendix C for a derivation)

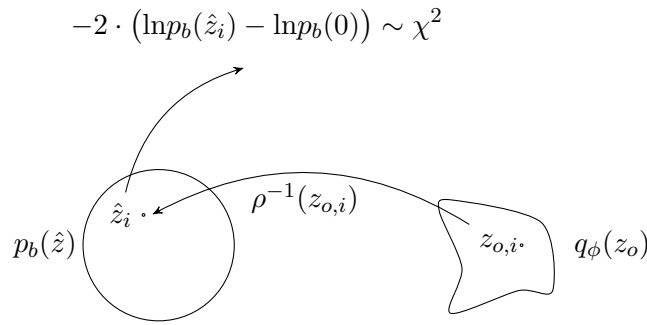
$$\rho_{\text{tot},1} = (\theta_1, \dots, \theta_{d-2}, \phi, \pi \cdot (1 - \text{erf}(r_g/\sqrt{2}))) \quad (d = 1) \quad (43)$$

$$\rho_{\text{tot},2} = (\theta_1, \dots, \theta_{d-2}, \phi, \arccos(1 - 2 \cdot \exp(-r_g^2/2))) \quad (d = 2) \quad (44)$$

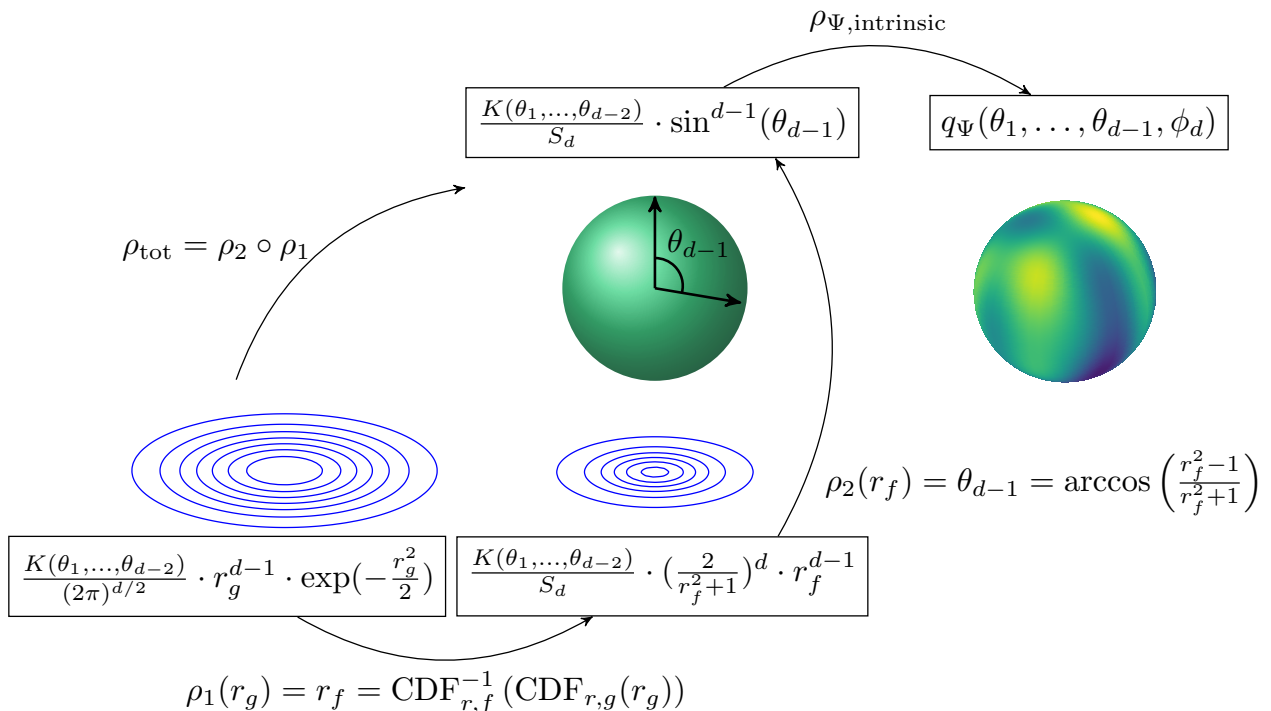
for the special cases of the 1-sphere and 2-sphere, respectively. For higher-dimensional spheres, no analytical function for the radial part can be written down, but individual sub-parts of the flow are analytical. Evaluations and inverses can be obtained using bisection and a potentially Newton iterations if derivatives are desired.

To demonstrate coverage, Fig. 8 (a)+(b) illustrate expected versus actual (a) and (b) coverage for learning a 2-d (position) and 3-d (position and 1-d direction) posterior in the supervised learning setting. The 2-d calculation employs a 2-dimensional Gaussianization flow [42] trained on dataset 2. The 3-d posterior is trained on dataset 3, in which as an additional degree of freedom also the direction of neutrino interactions is randomized. We use a factorized posterior $q_\phi(x_p, y_p, \theta; x) = q_{\phi_1}(x_p, y_p; x) \cdot q_{\phi_2}(\theta; x_p, y_p, x)$, which allows to learn the spherical part separately from the Euclidean part in a stable manner via an autoregressive structure [39]. While the Euclidean part again uses a 2-d Gaussianization flow, the spherical part employs the previously described strategy to reach a flat distribution on the 1-sphere (eq. 43) and afterwards uses convex Moebius transformations [49] parametrized by a neural network as an intrinsic flow. Coverage is calculated by transforming both inputs backwards to a joint 3-d standard normal distribution. This is an example for coverage of a joint posterior defined on $\mathbb{R}^2 \times \mathcal{S}^1$, but the methodology works analogously for general dimensions and more than two manifolds.

We can observe interesting coverage behavior during training. In both example cases, initially the posteriors either under- or over-cover. Once the first phase of training is over, in which the loss function decreases rapidly, good coverage is already reached, even though the overall training has not finished yet. The learning curves of the two training runs are depicted in Fig. 8 (c)+(d). The second phase, in which the optimization is much slower has been called "random diffusion phase" by [50]. The authors argue the network learns a better compression of the input data in this stage. In the context of normalizing flows, it seems the first phase brings the learned posteriors in line with the labels to reach proper coverage. In the second diffusion phase, the posterior regions shrink as much as they can while maintaining coverage.



(a) Illustration of χ^2 behavior in the base distribution.



(b) Illustration of a stable normalizing flow q_{Ψ} on the d -sphere starting with a d -dimensional standard normal distribution to allow for exact coverage calculation. The flows ρ_1 and ρ_2 involve only the radial coordinate due to rotational symmetry. The second flow ρ_2 is equal to the stereographic projection with a hyper plane that splits the sphere into two hemispheres. This is different from the visualization for illustrative purposes.

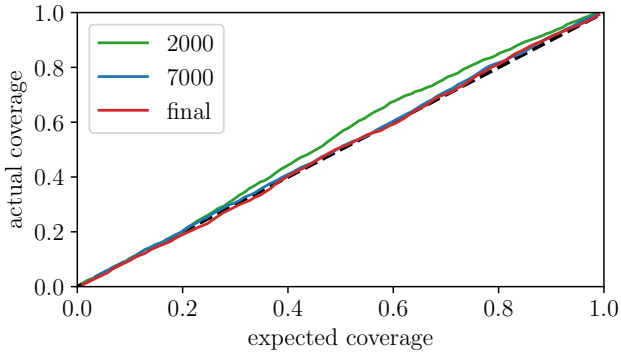
Figure 7: Coverage schematics to indicate the connection to the χ^2 distribution at the base distribution (a) and to indicate the discussed technique to calculate coverage for spherical distributions (b).

To illustrate the effect of systematic uncertainties on the resulting coverage, Fig. 8 (e) shows the coverage curve for a "systematic" dataset where the expected photon count in each module is marginalized with a Gaussian with a relative width of 50%. Including the systematic marginalization leads to slight over-coverage with respect to the true labels which is the desired behavior.

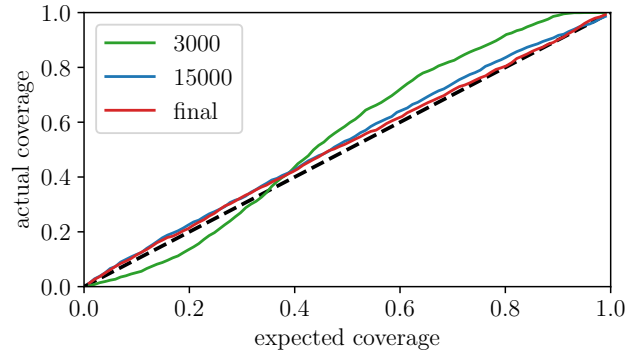
7 Goodness-of-Fit of the neural network model

The coverage calculation is only a meaningful information for data that is similar to the training data. If new input data is given to a fully trained neural network, for example real data instead of a Monte Carlo simulation, it is desirable to test if this new data can be described by the neural network model. If this is the case then the coverage results might apply⁴. Traditionally, a test between a model and data is done via a goodness-of-fit test. In the following we describe how the extended supervised training procedure described

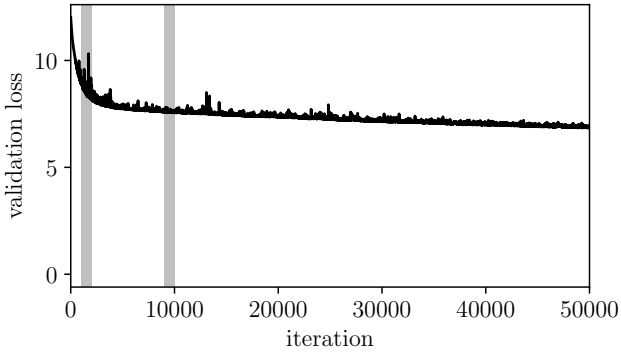
⁴We presume coverage is calculated using the validation dataset and that validation and training dataset are sufficiently similar.



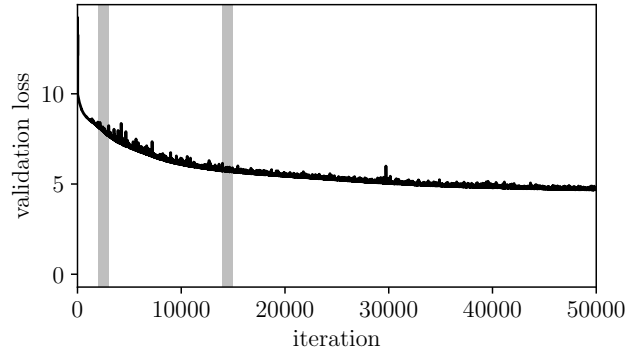
(a) Coverage of 3-d posteriors using dataset 3 for different stages of training.



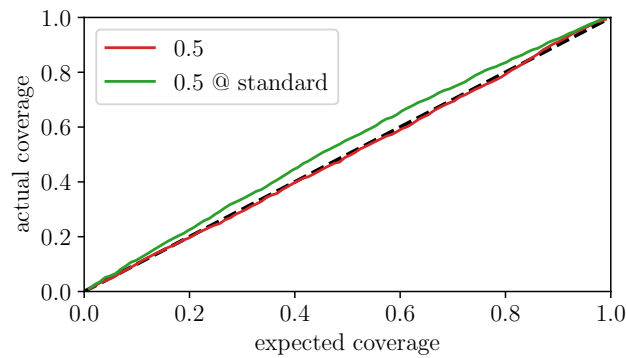
(b) Coverage of 2-d posteriors using dataset 2 for different stages of training.



(c) Validation loss curve for 3-d posteriors connected to (a).



(d) Validation loss curve for 2-d posteriors connected to (b).



(e) Coverage for a dataset trained on marginalized photon light yield expectation (red) and applied to a standard dataset (green).

Figure 8: Illustration of coverage for a 2-d (a) and 3-d (b) posterior calculated for the validation dataset. The respective learning curves are shown for 2-d (c) and 3-d (d), including intervals where the models are averaged using SWA for earlier coverage calculation in comparison to coverage obtained at the end of training (final). A coverage calculation for a marginalized systematic dataset is shown in (e) applied to itself (red) and a dataset with the true value of the systematic parameter (green).

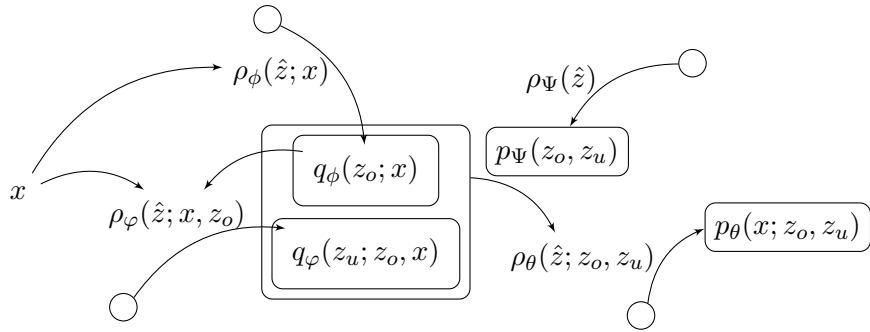


Figure 9: Generic structure of the extended supervised loss for goodness-of-fit tests and semi-supervised applications based on four normalizing flows. The respective auxiliary unit-Gaussian random variables \hat{z} are denoted by circles and the respective flow-defining functions by ρ .

in Section 2.3 allows to calculate a goodness-of-fit via posterior predictive checks. The structure of the extended supervised model is shown in Fig. 9. On top of a posterior q_ϕ , we have an additional posterior over unobserved latents q_φ , and a prior p_ψ and likelihood p_θ as a generative model. Posterior predictive checks are a standard methodology in Bayesian analysis to do goodness-of-fit tests of the resulting posterior distribution (see [51], chapter 6.3). In the extended supervised scheme, a posterior-predictive p-value, sometimes also called "Bayesian p-value" [51], can be defined via

$$p_{\text{val}} = \int_{x,z} \mathbf{I}_{T(x,z) > T(x_{\text{obs}}, z)} p_\theta(x; z) q_\phi(z; x_{\text{obs}}) dx dz \quad (45)$$

and numerically calculated using samples from $p_\theta(x; z) \cdot q_\phi(z; x_{\text{obs}})$, i.e. from the posterior predictive distribution. The quantities $T(x, z)$ are called test quantities, and $\mathbf{I}_{T(x,z) > T(x_{\text{obs}}, z)}$ the indicator function, where the integral effectively counts the fraction of samples where $T(x_i, z_i) > T(x_{\text{obs}}, z_i)$ for an infinite number of samples x_i, z_i . A comparison of a given p-value with the ensemble of p-values from the training dataset gives a goodness-of-fit criterion. In contrast to Frequentist goodness-of-fit testing, the test quantities also depend on the parameter z , and the p-value distribution of the true model can be non-uniform and is usually more peaked around 0.5 [51]. Only in certain limits, for example for infinitely precise posterior distributions, does the p-value distribution approach the uniform distribution [51]. In our case, we additionally do not expect to reach a uniform distribution as the neural network model will only yield an approximation of the true model, in particular since we do not have access to the exact likelihood function, but learn the likelihood in tandem with the posterior distribution. We therefore determine the null hypothesis p-value distribution from the training data distribution. We propose to use a normalized version of the logarithm of the likelihood (eq. 39)

$$T(x = (\bar{k}, \bar{t}), z) = \sum_{j=1}^N \frac{-\lambda_j(\theta) + k_j \cdot \ln(\lambda_j(\theta)) - \ln(k_j!)}{N} + \sum_{i=1}^{N_{\text{tot}}} \frac{\ln p_\theta(t_i; z)}{N_{\text{tot}}} \quad (46)$$

as a test quantity for the Poisson process data. The division by the number of detection modules N and number of total observed photons N_{tot} in the whole detector makes different realizations of the data comparable.⁵ For other likelihoods, or a test quantity based on the posterior distribution, this division would probably not be necessary. Any test quantity based on the likelihood or posterior can readily be calculated since they are part of the extended supervised training.

In order to illustrate the overall procedure, the extended supervised training is performed on dataset 4 (see table 1 for information on all datasets). It contains shower-like interactions in a detector consisting of 400 modules, where the interactions are constrained to lie within a certain containment region (the black dashed region in Fig. 12). The photon arrival time PDFs that appear in the likelihood function 39 are modeled by a 1-dimensional conditional normalizing flow that takes as extra information the position of each module. Additionally, the mean count expectations of the Poisson distributions are predicted, and together with the normalizing flow, allow to describe the complete likelihood function. Details are given in appendix B. The p-value distribution of the training dataset after training is shown in Fig. 10 as the orange curve. In addition, two other p-value distributions are depicted, where the final trained model is applied to events from dataset 5 (shower-like) and dataset 6 (track-like). Dataset 5 differs from dataset 4 in that it also consists of shower-like events outside the containment region. As can be seen, the p-value distribution for the training dataset is not totally uniform, possibly because it has not fully converged during training but more fundamentally it can really never describe the exact underlying true underlying model but only

⁵We also tested the default likelihood as a test quantity. However, the resulting p-value distribution is not as informative for a goodness-of-fit criterion due to larger fluctuations between realizations.

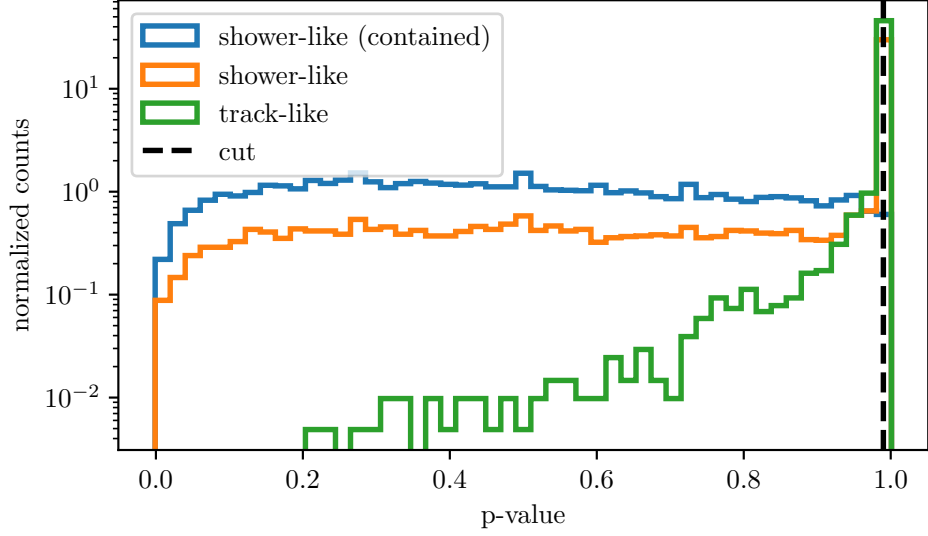


Figure 10: Goodness-of-fit p-value distribution for three datasets. The model is trained on a dataset which consists of contained shower-like neutrino interactions (dataset 4 - orange). The p-values are also calculated for a dataset of shower-like interactions in the whole detector (dataset 5 - blue) and a dataset consisting of 20 m long tracks of light emission (dataset 6 - green) to emulate muon tracks.

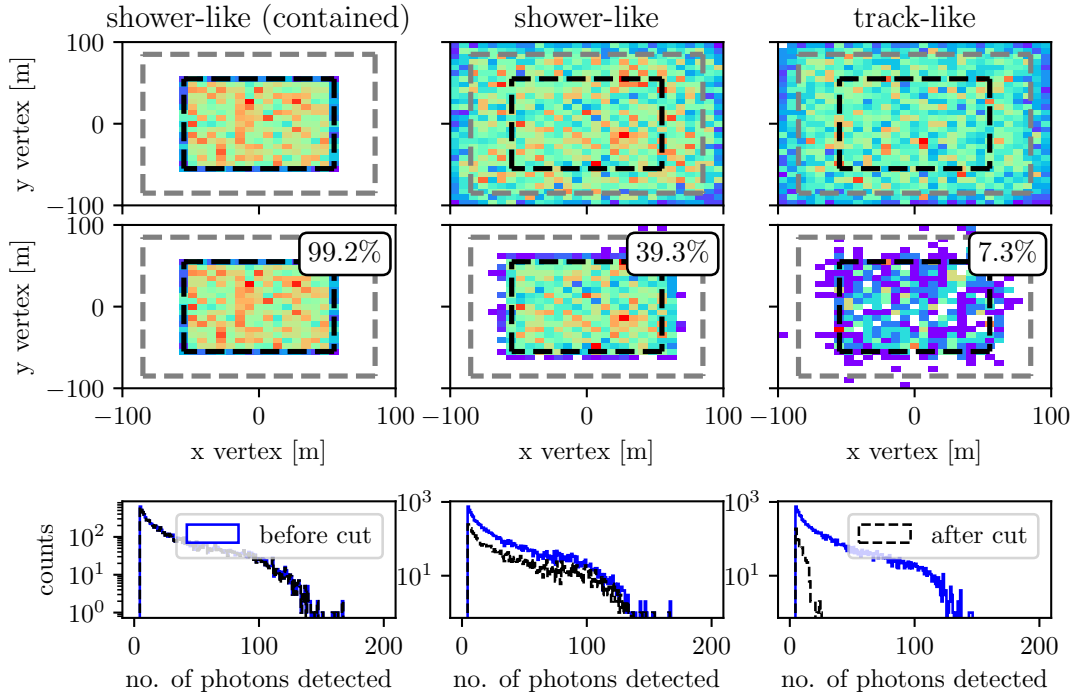


Figure 11: Effect of the p-value cut ($p_{\text{val}} < 0.99$) on the spatial distribution (upper row vs. center row) and the distribution of the number of detected photons (lower row) for datasets 4 to 6. The center row also indicates the percentage of retained events for the respective dataset.

an approximation to it. Dataset 5 has a similar shape, except it also contains a peak for p-values close to 1. The events that pile up close to 1 are events that lie outside the containment region, which are not part of the training dataset and therefore get such a bad goodness-of-fit. For dataset 6, which contains track-like events, there is a skew in the distribution which extends over the whole p-value range and most events have a p-value close to 1. Figure 11 shows the effect of applying a cut that retains events with a p-value smaller than 0.99. The training dataset is almost unchanged, while the cut removes most events outside the containment region for uncontained shower-like events. For track-like events, additionally events inside the detector are substantially reduced. The distribution of the number of photons per event in the lower row indicate that the events that remain for the track-like dataset are low energy events that have an intrinsically low information content and are with the given model not statistically separable to a low energy shower-like event. Therefore, a simple energy cut can remove those events and one would end up with a strong separation, in this example a complete background reduction above a certain energy threshold. An alternative is a cut on high-entropy events, which is possible with normalizing flows, since they allow to calculate the per-event differential entropy to arbitrary precision. This can also be seen in Fig. 12 b), which indicates two posterior distributions for the low- and high-energy shower, respectively. The latent variable takes on the fourth degree of freedom, which is proportional to the energy. The higher energy shower has a visibly lower overall entropy. This example is obtained with toy simulations that only qualitatively model a situation commonly encountered in neutrino telescopes, in particular with a 2-d compared to a 3-d setting. However, with 400 detection modules and the inclusion of relevant effects like scattering, absorption and typical Cherenkov emission features, the data should broadly mimic a real world world experiment like IceCube DeepCore[52] both in statistical and computational aspects. The result illustrates that it is in principle possible to train an extended supervised model on a signal dataset, apply the resulting model to any data event, and based on the resulting p-value decide to keep the event or exclude it from further analysis. The remaining events should be similar to events from the training sample, within uncertainties given by the training statistics and any included systematics. A further second cut on an energy variable or the entropy should then be enough to yield an optimal event selection for the given model. If the machine learning model is improved, for example by a better data encoding scheme or a more powerful normalizing flow, the p-value separation and thereby the final event selection should also improve. Besides such an application for data selection, it might also be interesting to study goodness-of-fit results for concrete data to Monte Carlo comparisons or for data anomaly detection.

8 Related Work

We discussed that standard supervised training can be viewed as variational inference, and variational inference can be viewed as an approximate likelihood-free inference approach. An active topic in likelihood-free inference are neural sequential inference procedures [53]. These procedures typically require guided re-simulations for a single event, and eventually should converge to the true posterior. From our perspective, simple supervised learning with normalizing flows, in combination with coverage and goodness-of-fit guarantees as described earlier, might be more suited for certain applications in high-energy physics or astro-particle physics where processing time is valuable - for example when posteriors for large amounts of data are desired. Also single astronomical multi-messenger alerts [10] can benefit. An initial posterior that can be trusted due to the discussed coverage and goodness-of-fit checks could be send to the community quickly. One can later always decide to refine the result with an iterative likelihood-free procedure like automatic posterior transformation (APT) [54] which would naturally blend in due to its use of normalizing flows. For gravitational waves, posterior inference with autoregressive flows has been discussed recently in [17]. In this line of work, coverage is checked with 1-dimensional marginal distributions which seems more computationally demanding than our approach. Systematics or goodness-of-fit tests are not discussed in that paper. In another related line of research, normalizing flows have been used to model the likelihood function directly [14]. Pure likelihood modeling inherits some problems of the standard likelihood machinery: a time consuming optimization or MCMC procedure. However, in our view it is useful to model the likelihood as the generative part in the proposed "extended supervised training" (Section 2.3), but always in combination with an associated posterior. A central part of our derivation is based on the joint KL-divergence. The importance of the joint KL-divergence has been emphasized in other approximate Bayesian inference, for example to unify expectation propagation in Gaussian processes [55] and as mentioned earlier for the derivation of the supervised loss for neural networks [19]. In the latter example, however, the loss function is not called the log-posterior, but conditional maximum likelihood objective with respect to the neural network parameters. While both views are correct, the posterior interpretation is more fruitful in our opinion, in particular in combination with normalizing flows which shows that supervised learning can behave as rather well-approximated variational inference. Another related recent work applied normalizing flows for a neutrino oscillation analysis [56]. The authors do not use the joint KL-divergence in the derivation, which makes it less obvious how to include systematics, although they briefly mention one approach among two alternatives that is similar to our suggestion. The authors also argue for a vague agreement of the base distribution with a Gaussian after training, but do not discuss quantifiable coverage tests.

Likelihood approaches typically only allow to define a rigorous goodness-of-fit for special random variables. However, realistic applications typically involve unbinned likelihoods, for which no rigorous goodness-of-fit can be defined [57]. Furthermore, coverage and systematics checks are often computationally challenging. For traditional machine learning based regression, and even for other methods with normalizing flows, as pointed out above, coverage or goodness-of-fit are either impossible or not straightforward to compute.

The proposed extended supervised training with conditional normalizing flows combines 1) systematics 2) coverage and 3) a rigorous goodness-of-fit measure in one variational inference algorithm, without restrictions to the underlying PDFs. We are not aware of any other Ansatz in the literature that has these properties.

9 Conclusion

In the first part of the paper we have shown that the supervised learning loss, an extended supervised loss and the unsupervised ELBO-loss of variational autoencoders can all be derived under one unifying theme of variational inference. The inference in all these approaches can be traced back to the minimization of the KL-divergence between the true joint distribution of data and labels and an approximation for certain sub-parts of the joint distribution based on neural networks.

For supervised learning, the derivation of the loss function from the KL-divergence of the joint distribution is well-known but the connection to variational inference of the posterior distribution is typically not being made. From our perspective, however, this interpretation is very useful in high-energy physics, even when using an MSE loss function which has very poor approximating power. After all, a central task of a physics analysis is to calculate a posterior distribution, and the variational perspective shows that neural networks learn to predict exactly that. Conditional amortized normalizing flows with a standard normal base naturally generalize the MSE loss, and are crucial to make the variational inference perspective usable in practice.

A simple replacement of observed with unobserved labels in the KL-divergence allows to eventually derive the ELBO loss of variational autoencoders. In this derivation, the usual encoder q_ϕ and decoder p_θ are both manifestly auxiliary, and are explicitly separated from the true distribution \mathcal{P}_t which p_θ and q_ϕ both try to approximate within a given identifiability class of transformations. This is different from the usual derivation via the marginal likelihood, e.g. as discussed in the original VAE paper [23], where p_θ is often used to denote both the true posterior and the recognition model, which obfuscates the fact that those are typically not the same and also do not have to be the same parametric class.

Conditional normalizing flows with a Gaussian base distribution have a second advantage. They can be used to calculate coverage for the n -dimensional probability density function $q_\phi(z_o; x)$ they describe. Transforming a test input back to the base distribution, $\hat{z}_i = \rho^{-1}(z_{o,i})$, allows to calculate the quantity $\lambda_{\text{base}} = -2 \cdot (\ln p_b(\hat{z}_i) - \ln p_b(0))$ which is χ_n^2 distributed if the input follows $q_\phi(z_o; x)$. A similar procedure is known from classical Frequentist coverage calculations under the assumption Wilks' theorem holds. In contrast, the normalizing-flow coverage calculation works for arbitrary posterior distributions $q_\phi(z_o; x)$ without any extra assumptions. We further expanded the idea to calculate coverage for arbitrary distributions on m -spheres \mathcal{S}^m , or more generally to posteriors defined autoregressively on tensor products like $\mathbb{R}^n \times \mathcal{S}^m$. To enable coverage for such distributions we derived the transformation from the m -dimensional standard normal Gaussian to the flat distribution on the m -sphere, which for 1 and 2 dimensions is conveniently simple and invertible. A further intrinsic flow on the sphere can then describe a more complex distribution. This two-step procedure ensures stable training, since starting with the flat distribution on the sphere is a more stable training process than deforming a distribution in the plane and afterwards stereographically project it, as was already pointed out in [49].

We demonstrated such a coverage calculation with a 2-d posterior of position x, y and with a joint 3-d posterior of position and direction x, y, θ for shower-like neutrino interactions in a 2-d toy Monte Carlo. Empirically, we observed that coverage is already obtained once the training phase enters the random diffusion phase as defined by [50]. Since the loss still decreases during this phase, only more slowly, and in the variational interpretation this implies shrinking posteriors, in this second training phase the posterior approximations get slowly better while coverage stays intact.

Viewing all these models as coming from the joint KL-divergence makes it also natural to include systematic uncertainties in the final approximated posterior distributions. They are included via Bayesian marginalization of the true posterior which can be included during the Monte Carlo generation process. We test the result with a coverage calculation for a dataset where the number of expected observed photons is marginalized with a Gaussian to emulate a systematic uncertainty. The resulting posterior regions are larger which leads to the desired over-coverage with respect to the original dataset.

Finally, we test the *extended supervised learning* scheme. It is related to semi-supervised learning and involves a hybrid of the supervised and VAE loss functions. In addition to the label posterior q_φ , a latent posterior q_ϕ , a prior p_ψ , and a decoder p_θ are learned either jointly or separately as an add-on to the supervised posterior q_φ . The extra distribution q_ϕ learns latent variables to describe information not captured by the posterior of known labels q_φ , while the prior and decoder define a generative model. The combination of a posterior and a generative model allows to perform Bayesian predictive simulations, which in combination with a test quantity $T(x, z)$, which we suggest to be the (reduced) log-likelihood function, allows to calculate

a p-value which can be used as a goodness-of-fit criterion. Any data that are not similar to the training data within the given uncertainty of the statistical approximations of the neural networks lead to p-values close to 1 and can be excluded. We test this concept with a neural network model trained on shower-like neutrino interactions contained in the center of a hypothetical detector consisting of 400 detection modules. In comparison with shower-like interactions in the full detector, the model calculates a small p-value for events on the boundary of the detector. We also apply it on a dataset containing track-like energy depositions mimicking muon tracks, for which the separation is markedly visible. Such a goodness-of-fit selection strategy can potentially allow a very simple data selection. Any data which is sufficiently different from the training data can be removed by a simple selection based on the p-value and second cut based on energy or entropy of the posterior distribution.

Let us mention two aspects that require further investigation. The first is related to the stability of the training algorithm and the final learned distributions. We used stochastic weight averaging to average over several iterations at the end of training to obtain a more stable posterior solution. This serves as an approximation to ensemble averaging, which is basically averaging under a variational posterior over network weights. Due to varying learning rates for different model complexities, slight fluctuations in the final loss values remained (see Fig. 5). Ideally, one would like a scheme where repeated training schedules lead to repeatable posterior regions which are indistinguishable within a certain margin which can be defined before training. This needs to be studied more systematically.

A second aspect is related to the data encoding. In all studies we have split the conditional posterior into a data encoding based on a GRU and aggregate MLP, and a second MLP which further maps that encoding summary to the normalizing-flow parameters. Our Monte Carlo tests show that at some level of flow complexity the performance bottleneck of the posterior approximation can in part stem from the data-encoding architecture. This particular encoding was only chosen for simplicity and serves the demonstrative purposes, but it is very likely that it is not an optimal encoding. It will therefore be interesting to study more powerful encoding strategies, and potentially identify an optimal encoding for Poisson process data, which is an important data type in (astro-)particle physics. Any improvement in data encoding will not only translate to tighter posterior contours, but also to a more powerful goodness-of-fit calculation.

Acknowledgements

We thank Alexander Trettin for suggesting a more realistic parametrization for the toy Monte Carlo.

Code Availability

In the course of this work a software package has been developed to handle the described product manifold normalizing flows and allow for straightforward coverage calculations. It is available as an open-source software package at https://github.com/thoglu/jammy_flows.

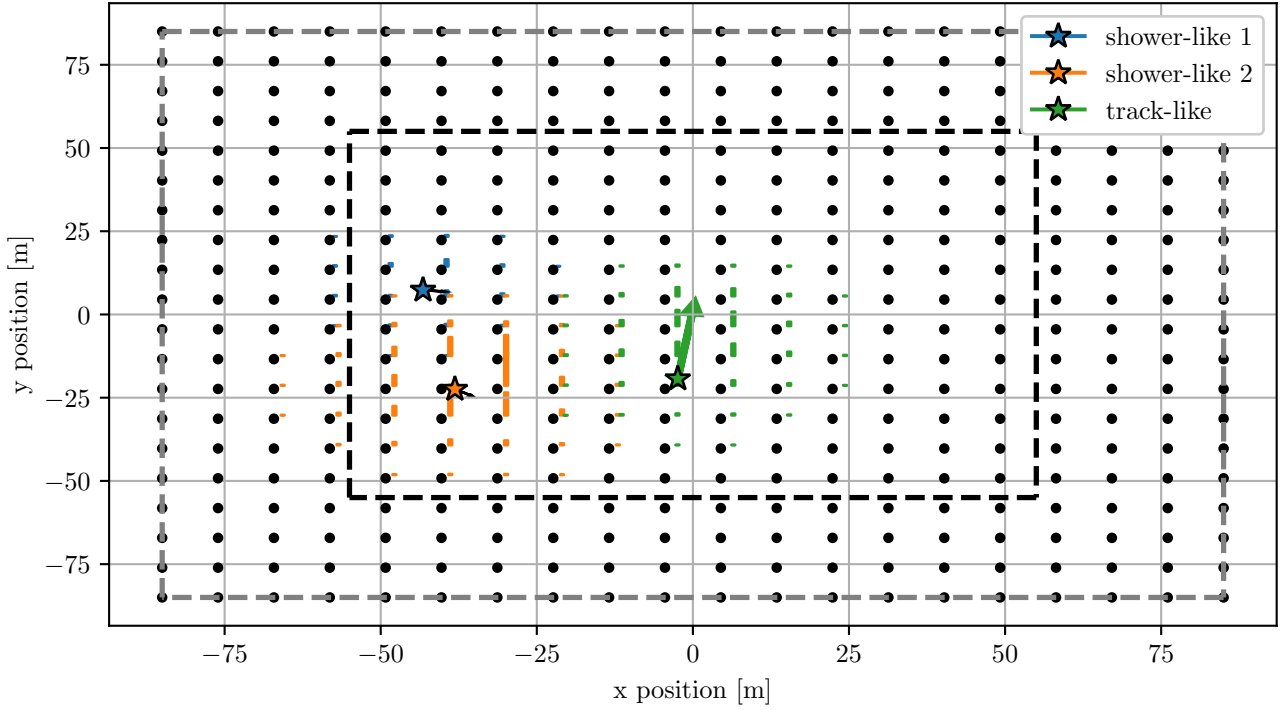
A Supplementary material for goodness-of-fit simulation

Figure 12 a) shows the interaction of three example events involved in the goodness-of-fit tests from Section 7. The first two events are a low energy (blue) and high-energy (orange) shower event from dataset 4. The third event is a 20 m track-like event (green) from dataset 6 (see table 1 for a list of all datasets). All three events are within the containment volume, as defined by dataset 4 ("contained showers"), which is also indicated as the black bounding box. Figure 12 b) shows a comparison of the final posterior distributions of the two shower events over the four dataset degrees of freedom after training. The energy is not used as a label during training, so the latent variable from the unsupervised part of the extended supervised training can be identified with the energy degree of freedom. The high-energy shower (orange) produces more photons, and allows to better inform about the true event properties than the lower energy shower.

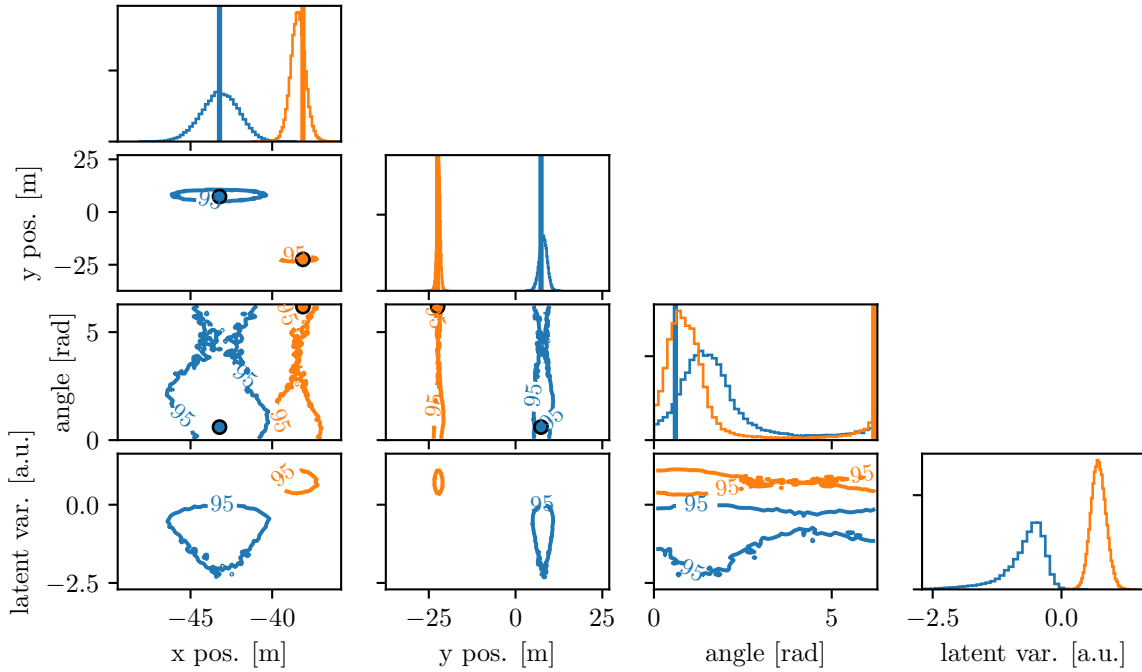
B Implementation details

B.1 Training

All training procedures use ADAM [58], which gives much faster convergence than standard gradient descent (SGD) [59]. We use a mostly fixed learning rate which adjusts itself to keep fluctuations of the validation loss at a certain level. For the affine flows, we had to fix the learning rate completely, because too large learning rates would sometimes lead to drastic jumps in the loss function. This seems to be a problem that only occurs for flows which are defined by less than a handful of parameters. For Gaussianization flows [42], similar behavior could be seen for single-layer flows with a single basis function. Once the number of flow parameters is increased beyond a certain level, it does not seem to be an issue anymore. Towards the end of training, once the loss reaches a more or less constant level, the final iterations are averaged using



(a) Example interactions of three events overlaid on the detector used in datasets 4 – 6. Detector modules are denoted as black dots. The relative expected photon count in each module is visualized as vertical bars with the respective color.



(b) Visualization of the final posterior approximation contours (1d and 2d marginals) for the two shower-like events visualized in Fig. 12 a). The Monte Carlo truth is indicated with markers and vertical lines.

Figure 12: A few events from the datasets for the goodness-of-fit example.

stochastic weight averaging (SWA) [41]. As argued by the authors, SWA approximates model ensemble averages. Model averages, in turn, can be used to calculate the expectation value under the approximate weight posterior since SGD iterations itself can be interpreted as samples from a variational approximation of the weight posterior [60].

B.2 Posterior

The posterior parametrization is indicated in Fig. 3 (c). The first encoding part is similar for all experiments. A GRU encodes the input data sequentially, the output is aggregated and mapped by a single layer MLP to a representation h that summarizes the data.

The second step in the posterior is another MLP that maps the summary representation h to the respective flow parameters. We use two inner layers for this second MLP, and vary its number of dimensions for the various experiments. The parameter choices are described in Section B.4.

B.3 Likelihood

For the goodness-of-fit likelihood, we use a normalizing flow for the continuous part of the Poisson process likelihood (eq. 39). The involved MLP that is used in the amortization also outputs a logarithmic mean expectation for photon counts to calculate the related Poisson distribution. By simultaneously predicting the flow parameters and the Poisson mean, it is possible to model the correlation between the two. The input to the MLP are the labels and the module position in (x,y) coordinates.

B.4 Parameter choices

We choose a single-layer GRU with hidden dimension 10 and for the aggregation MLP choose intermediate dimension 15 and map to a 20-dimensional representation h for the first 3 datasets in the paper. This encoding part then has roughly 1000 parameters. For the larger detector used in datasets 4-6 the involved dimensions are a bit larger. For the comparison in Fig. 5 the dimensions in the two inner layers of the second MLP vary between 1 and 100. For the Gaussianization flow, additionally the number of flow layers varies between 1 and 5, and the number of basis elements per flow varies between 1 and 10, as the flow complexity increases.

C Coverage for spheres

The following calculation derives the transformation ρ_{tot} from the d-dimensional Gaussian distribution to the flat distribution on the d-sphere (see Fig. 7 b)) which is discussed in Section 6. The flow can be split up as $\rho_{\text{tot}} = \rho_2 \circ \rho_1$. The first flow ρ_1 transforms the standard normal to a distribution p_f that corresponds to the distribution in the plane that is the stereographic projection of the flat distribution on the sphere. We can derive p_f by starting with the flat distribution on the sphere. The flat distribution on the d-sphere is defined as [61]

$$p_{\text{flat,sphere}} = \frac{\sin(\theta_1)^1 \cdot \dots \cdot \sin(\theta_{d-1})^{d-1}}{S_d} = \frac{K(\theta_1, \dots, \theta_{d-2}) \cdot \sin(\theta_{d-1})^{d-1}}{S_d} \quad (47)$$

where the sine factors start to appear at dimension two. The factor K abbreviates the first $d-2$ of those factors and S_d denotes the surface area of the d-sphere. Note that θ_1 to θ_{d-1} take values between 0 and π , and an additional angle ϕ takes values between 0 and 2π . We then define a flow $\rho_2^{-1} = (\theta_1, \dots, \theta_{d-2}, \phi, \rho_2^{-1}(\theta_{d-1}))$ which is similar to a stereographic projection to the plane and which just transforms the last spherical coordinate θ_{d-1} , while all other angles are left unchanged. The angle θ_{d-1} is always related to the d th embedding space coordinate x_d via $x_d = \cos(\theta_{d-1})$ ⁶. In 3-dimensional space, for example, x_d equals the z coordinate. At the same time, for a stereographic projection onto a plane which aligns to split the sphere and has plane coordinates \mathbf{x}_p , it is known [62] that the relation of the embedding coordinate x_d to the plane coordinates is given by $x_d = \frac{(\sum x_{p,j})^2 - 1}{(\sum x_{p,j})^2 + 1} = \frac{r_f^2 - 1}{r_f^2 + 1}$, which is expressed here entirely as a connection to the radial coordinate in the plane via $r_f = \sum x_{p,j}$. It therefore follows that

$$\theta_{d-1} = \arccos\left(\frac{r_f^2 - 1}{r_f^2 + 1}\right) \equiv \rho_2(r_f) \quad (48)$$

or vice versa

$$r_f = \sqrt{\frac{2}{1 - \cos(\theta_{d-1})}} - 1 \equiv \rho_2^{-1}(\theta_{d-1}) \quad (49)$$

⁶Note that for $d=1$ the angle ϕ , which normally is defined with respect to $(1,0)$ and goes from 0 to 2π , has to be redefined as $\theta_0 = \phi + \frac{\pi}{2}$ in order for this relation to hold. The angle θ_0 further goes from 0 to π , similar to the other θ_{d-1} , and is measured with respect to the "north pole" of the sphere.

which is a relation that is indicated in Fig. 7 b). Applying the flow ρ_2^{-1} to the flat distribution on the sphere we obtain

$$p_f(\theta_1, \dots, \theta_{d-2}, \phi, r_f) = p_{\text{flat, sphere}}(\theta_1, \dots, \theta_{d-2}, \phi, \rho_2(r_f)) \cdot \left| \frac{d\rho_2(r_f)}{d\theta_{r_f}} \right| \quad (50)$$

$$= \frac{K(\theta_1, \dots, \theta_{d-2})}{S_d} \cdot \left(1 - \left(\frac{r_f^2 - 1}{r_f^2 + 1} \right)^2 \right)^{(d-1)/2} \cdot \frac{2}{r_f^2 + 1} \cdot r_f^{d-1} \quad (51)$$

$$= \frac{K(\theta_1, \dots, \theta_{d-2})}{S_d} \cdot \left(\frac{2}{r_f^2 + 1} \right)^d \cdot r_f^{d-1} \quad (52)$$

where p_f is now the corresponding PDF in the plane after the stereographic projection. We now need to find the flow ρ_1 (indicated in Fig. 7 b) to transform a standard normal Gaussian distribution to p_f or vice versa. Similar to the transformation from the sphere to plane, this transformation can be done entirely in the radial coordinate when the Gaussian distribution is written in spherical coordinates. The radial transformation can be calculated using the cumulative distribution functions of the radial PDFs. The two radial PDFs are

$$p_{r,g}(r_g) = \int_{\theta_1, \dots, \theta_{d-2}, \phi} \frac{K(\theta_1, \dots, \theta_{d-2})}{(2\pi)^{d/2}} \cdot r_g^{d-1} \cdot \exp\left(-\frac{r_g^2}{2}\right) d\theta_1 \dots d\theta_{d-2} d\phi \quad (53)$$

$$= \frac{S_{d-1}}{(2\pi)^{d/2}} r_g^{d-1} \cdot \exp\left(-\frac{r_g^2}{2}\right) \quad (54)$$

and

$$p_{r,f}(r_f) = \int_{\theta_1, \dots, \theta_{d-2}, \phi} \frac{K(\theta_1, \dots, \theta_{d-2})}{S_d} \cdot \left(\frac{2}{r_f^2 + 1} \right)^d \cdot r_f^{d-1} d\theta_1 \dots d\theta_{d-2} d\phi \quad (55)$$

$$= \frac{S_{d-1}}{S_d} \cdot \left(\frac{2}{r_f^2 + 1} \right)^d \cdot r_f^{d-1} \quad (56)$$

where $p_{r,g}$ is the radial distribution of the d-dimensional standard normal distribution and $p_{r,f}$ the radial distribution of p_f . The corresponding CDFs which map from \mathbb{R}^+ to $[0, 1]$ then follow to be ⁷

$$\text{CDF}_{r,g} = \frac{S_{d-1}}{2 \cdot (\pi)^{d/2}} \cdot (\Gamma(d/2) - \Gamma(d/2, r_g^2/2)) \quad (\text{general } d) \quad (57)$$

$$\text{CDF}_{r,g,1} = \text{erf}(r_g/\sqrt{2}) \quad (d = 1) \quad (58)$$

$$\text{CDF}_{r,g,2} = 1 - \exp(-r_g^2/2) \quad (d = 2) \quad (59)$$

and

$$\text{CDF}_{r,f} = \frac{S_{d-1} \cdot (2 \cdot r_f)^d}{S_d \cdot d} \cdot {}_2F_1(d/2; d; d/2 + 1; -r_f^2) \quad (\text{general } d) \quad (60)$$

$$\text{CDF}_{r,f,1} = \frac{2}{\pi} \cdot \tan^{-1}(r_f) \quad (d = 1) \quad (61)$$

$$\text{CDF}_{r,f,2} = \frac{r_f^2}{r_f^2 + 1} \quad (d = 2) \quad (62)$$

where $\Gamma(x, y)$ is the upper incomplete Gamma function and ${}_2F_1$ is the Gauss hypergeometric function. The transformation ρ_1 then can be written with the corresponding CDFs as

$$r_f = \rho_1(r_g) = \text{CDF}_{r,f}^{-1}(\text{CDF}_{r,g}(r_g)) \quad (63)$$

which can in general not be written down analytically except for $d = 1$ and $d = 2$. Using bisection and Newton iterations it is possible to evaluate this expression and its inverse for higher d . The Newton iterations make the result differentiable, which is required if it is to be used in variational autoencoders. Finally, the transformation $\rho_{\text{tot}} = \rho_2 \circ \rho_1$ can be written as

$$\theta_{d-1} = \rho_{\text{tot}}(r_g) = \rho_2 \left(\text{CDF}_{r,f}^{-1}(\text{CDF}_{r,g}(r_g)) \right) \quad (\text{general } d) \quad (64)$$

$$\rho_{\text{tot},1}(r_g) = \pi \cdot (1 - \text{erf}(r_g/\sqrt{2})) \quad (d = 1) \quad (65)$$

⁷The general formula is evaluated using *Wolfram Alpha* at <http://www.wolfram-alpha.com>. The calculation of $\text{CDF}_{r,g}$ likely involves variable substitution, integration by parts, and then an identification with the upper incomplete gamma function. The calculation of $\text{CDF}_{r,f}$ likely involves variable substitution and an iterative application of hypergeometric identities.

$$\rho_{\text{tot},2}(r_g) = \arccos(1 - 2 \cdot \exp(-r_g^2/2)) \quad (d = 2) \quad (66)$$

$$(67)$$

, which has a simple and invertible structure for $d = 1$ and $d = 2$ after some manipulation with trigonometric identities, while higher dimensions again require bisection and Newton iterations. Because ρ_{tot} defines a flow from the d -dimensional standard normal distribution to the flat distribution on the d -sphere, besides its usage in normalizing flows for coverage as describe in Section 6, it can be used as a non-standard way to generate uniform samples on the d -sphere. This can be done by first sampling from the d -dimensional standard normal distribution, switching to spherical coordinates, and finally transforming the radial coordinate to the last coordinate θ_{d-1} on the sphere using ρ_{tot} , while keeping all other angles $\theta_1, \dots, \theta_{d-2}$ and ϕ as they are.

References

- [1] Krizhevsky, A., Sutskever, I. & Hinton, G. E. Imagenet classification with deep convolutional neural networks. In *Advances in Neural Information Processing Systems*, vol. 25, 1097–1105 (2012).
- [2] Guest, D., Cranmer, K. & Whiteson, D. Deep learning and its application to LHC physics. *Annual Review of Nuclear and Particle Science* **68**, 161–181 (2018). [arXiv:1806.11484](#).
- [3] Komiske, P. T., Metodiev, E. M. & Schwartz, M. D. Deep learning in color: towards automated quark/gluon jet discrimination. *JHEP* **01**, 110 (2017). [arXiv:1612.01551](#).
- [4] Murach, T., Gajdus, M. & Parsons, R. D. A neural network-based monoscopic reconstruction algorithm for H.E.S.S. II. In *ICRC2015*, 1022 (2016). [arXiv:1509.00794](#).
- [5] Ahrens, J. *et al.* Muon track reconstruction and data selection techniques in AMANDA. *Nucl. Instrum. Meth. A* **524**, 169–194 (2004). [arXiv:astro-ph/0407044](#).
- [6] Roe, B. P. *Probability And Statistics In Experimental Physics* (Springer Science & Business Media, 2012).
- [7] Aartsen, M. G. *et al.* Cosmic ray spectrum and composition from PeV to EeV using 3 years of data from IceTop and IceCube. *prd* **100**, 082002 (2019). [arXiv:1906.04317](#).
- [8] Aartsen, M. *et al.* The IceCube Neutrino Observatory: instrumentation and online systems. *Journal of Instrumentation* **12**, P03012 (2017). [arXiv:1612.05093](#).
- [9] Abbott, B. *et al.* Ligo: the laser interferometer gravitational-wave observatory. *Reports on Progress in Physics* **72**, 076901 (2009). [arXiv:0711.3041](#).
- [10] Keivani, A. *et al.* Multi-messenger gravitational-wave + high-energy neutrino searches with LIGO, Virgo and IceCube. In *36th International Cosmic Ray Conference (ICRC2019)*, vol. 36 of *International Cosmic Ray Conference*, 930 (2019). [arXiv:1908.04996](#).
- [11] Jospin, L. V., Laga, H., Boussaid, F., Buntine, W. & Bennamoun, M. Hands-on bayesian neural networks—a tutorial for deep learning users. *IEEE Computational Intelligence Magazine* **17**, 29–48 (2022). [arXiv:2007.06823](#).
- [12] Gal, Y. & Ghahramani, Z. Dropout as a bayesian approximation: Representing model uncertainty in deep learning. In *Proceedings of the 33rd International Conference on International Conference on Machine Learning*, vol. 48 of *ICML'16* (2016). [arXiv:1506.02142](#).
- [13] Lakshminarayanan, B., Pritzel, A. & Blundell, C. Simple and Scalable Predictive Uncertainty Estimation using Deep Ensembles. In *Advances in Neural Information Processing Systems*, 6402–6413 (2017). [arXiv:1612.01474](#).
- [14] Wong, K. W., Contardo, G. & Ho, S. Gravitational-wave population inference with deep flow-based generative network. *Phys. Rev. D* **101**, 123005 (2020). [arXiv:2002.09491](#).
- [15] Gilks, W. R., Spiegelhalter, D. & Richardson, S. *Markov Chain Monte Carlo in Practice* (American Cancer Society, 1995).
- [16] Chua, A. J. K. & Vallisneri, M. Learning Bayesian posteriors with neural networks for gravitational-wave inference. *Phys. Rev. Lett.* **124**, 041102 (2020). [arXiv:1909.05966](#).
- [17] Green, S. R., Simpson, C. & Gair, J. Gravitational-wave parameter estimation with autoregressive neural network flows. *Phys. Rev. D* **102**, 104057 (2020). [arXiv:2002.07656](#).

- [18] Kullback, S. & Leibler, R. On information and sufficiency. *Ann. Math. Statist.* **22**, 79–86 (1951).
- [19] Martens, J. New insights and perspectives on the natural gradient method. *Journal of Machine Learning Research* **21**, 1–76 (2020). [arXiv:1412.1193](#).
- [20] Kobyzev, I., Prince, S. & Brubaker, M. Normalizing flows: An introduction and review of current methods. *IEEE Transactions on Pattern Analysis and Machine Intelligence* 1–1 (2020). [arXiv:1908.09257](#).
- [21] Blei, D. M., Kucukelbir, A. & McAuliffe, J. D. Variational inference: A review for statisticians. *Journal of the American Statistical Association* **112**, 859–877 (2017). [arXiv:1601.00670](#).
- [22] Whitehorn, N., van Santen, J. & Lafebre, S. Penalized splines for smooth representation of high-dimensional Monte Carlo datasets. *Comput. Phys. Commun.* **184**, 2214–2220 (2013). [arXiv:1301.2184](#).
- [23] Kingma, D. & Welling, M. Auto-Encoding Variational Bayes. In *2nd International Conference on Learning Representations* (2014). [arXiv:1312.6114](#).
- [24] Steuer, R., Kurths, J., Daub, C. O., Weise, J. & Selbig, J. The Mutual Information: Detecting and evaluating dependencies between variables. *Bioinformatics* **18**, S231–S240 (2002).
- [25] Rényi, A. On measures of entropy and information. In *Proceedings of the fourth Berkeley Symposium on Mathematics, Statistics and Probability*, 547–561 (1960).
- [26] Zhao, S., Song, J. & Ermon, S. InfoVAE: Balancing learning and inference in Variational Autoencoders. In *The Thirty-Third AAAI Conference on Artificial Intelligence (AAAI)* (2019). [arXiv:1706.02262](#).
- [27] Zhao, S., Song, J. & Ermon, S. The information autoencoding family: A lagrangian perspective on latent variable generative models. *arXiv preprint* (2018). [arXiv:1806.06514](#).
- [28] Jordan, M. I., Ghahramani, Z., Jaakkola, T. S. & Saul, L. K. An introduction to variational methods for graphical models. *Mach. Learn.* **37**, 183–233 (1999).
- [29] Khemakhem, I., Kingma, D., Monti, R. & Hyvarinen, A. Variational autoencoders and nonlinear ICA: A unifying framework. In *International Conference on Artificial Intelligence and Statistics*, 2207–2217 (2020). [arXiv:1907.04809](#).
- [30] Kim, H. & Mnih, A. Disentangling by factorising. In Dy, J. & Krause, A. (eds.) *Proceedings of the 35th International Conference on Machine Learning*, vol. 80 of *Proceedings of Machine Learning Research*, 2649–2658 (PMLR, 2018). [arXiv:1802.05983](#).
- [31] Tomczak, J. & Welling, M. Vae with a VampPrior. In *Proceedings of the 35th International Conference on Machine Learning*, vol. 84 of *Proceedings of Machine Learning Research*, 1214–1223 (PMLR, 2018). [arXiv:1705.07120](#).
- [32] Higgins, I. *et al.* beta-VAE: Learning basic visual concepts with a constrained variational framework. *ICLR17* (2017).
- [33] Tanabashi, M. & *et al.* Review of particle physics. *Phys. Rev. D* **98**, 030001 (2018).
- [34] Radel, L. & Wiebusch, C. Calculation of the Cherenkov light yield from electromagnetic cascades in ice with Geant4. *Astropart. Phys.* **44**, 102–113 (2013). [arXiv:1210.5140](#).
- [35] Kutoyants, Y. A. *Statistical Inference for Spatial Poisson Processes* (Springer, 1998).
- [36] Barlow, R. Extended maximum likelihood. *Nuclear Instruments and Methods in Physics Research Section A: Accelerators, Spectrometers, Detectors and Associated Equipment* **297**, 496–506 (1990).
- [37] Rezende, D. J. & Mohamed, S. Variational inference with normalizing flows. ICML’15, 1530–1538 (JMLR, 2015). [arXiv:1505.05770](#).
- [38] Aiello, S. *et al.* Event reconstruction for KM3NeT/ORCA using convolutional neural networks. *JINST* **15**, P10005 (2020). [arXiv:2004.08254](#).
- [39] Kingma, D. P. *et al.* Improved variational inference with inverse autoregressive flow. In *Proceedings of the 30th International Conference on Neural Information Processing Systems, NIPS’16*, 4743–4751 (2016). [arXiv:1606.04934](#).
- [40] Cho, K., Van Merriënboer, B., Bahdanau, D. & Bengio, Y. On the properties of neural machine translation: Encoder-decoder approaches. In *Eighth Workshop on Syntax, Semantics and Structure in Statistical Translation* (2014). [arXiv:1409.1259](#).

- [41] Izmailov, P., Podoprikin, D., Garipov, T., Vetrov, D. & Wilson, A. G. Averaging weights leads to wider optima and better generalization. In *Conference on Uncertainty in Artificial Intelligence* (2018). 1803.05407.
- [42] Meng, C., Song, Y., Song, J. & Ermon, S. Gaussianization flows. In *Proceedings of the Twenty Third International Conference on Artificial Intelligence and Statistics*, vol. 108 of *Proceedings of Machine Learning Research*, 4336–4345 (PMLR, 2020).
- [43] Cranmer, K. Practical statistics for the LHC. *CERN-2014-003* 267 – 308 (2011). [arXiv:1503.07622](#).
- [44] Aartsen, M. *et al.* Efficient propagation of systematic uncertainties from calibration to analysis with the SnowStorm method in IceCube. *Journal of Cosmology and Astroparticle Physics* **2019**, 048 (2019).
- [45] Wilks, S. S. The large-sample distribution of the likelihood ratio for testing composite hypotheses. *Ann. Math. Statist.* **9**, 60–62 (1938).
- [46] Vaart, A. W. v. d. *Asymptotic Statistics*. Cambridge Series in Statistical and Probabilistic Mathematics (Cambridge University Press, 1998).
- [47] Cowan, G. *Statistical data analysis* (Oxford university press, 1998).
- [48] Gemici, M. C., Rezende, D. & Mohamed, S. Normalizing Flows on Riemannian Manifolds. *arXiv preprint* (2016). [arXiv:1611.02304](#).
- [49] Rezende, D. J. *et al.* Normalizing flows on tori and spheres. In *Proceedings of the 37th International Conference on Machine Learning*, vol. 119 of *Proceedings of Machine Learning Research*, 8083–8092 (PMLR, 2020). [arXiv:2002.02428](#).
- [50] Shwartz-Ziv, R. & Tishby, N. Opening the black box of deep neural networks via information. *arXiv preprint* (2017). [arXiv:1703.00810](#).
- [51] Gelman, A., Carlin, J. B., Stern, H. S. & Rubin, D. B. *Bayesian Data Analysis* (Chapman and Hall/CRC, 2004).
- [52] Abbasi, R. *et al.* The design and performance of IceCube DeepCore. *Astroparticle Physics* **35**, 615–624 (2012). [arXiv:1109.6096](#).
- [53] Papamakarios, G., Sterratt, D. & Murray, I. Sequential neural likelihood: Fast likelihood-free inference with autoregressive flows. In *Proceedings of Machine Learning Research*, vol. 89 of *Proceedings of Machine Learning Research*, 837–848 (PMLR, 2019). [arXiv:1805.07226](#).
- [54] Greenberg, D., Nonnenmacher, M. & Macke, J. Automatic posterior transformation for likelihood-free inference. In *Proceedings of the 36th International Conference on Machine Learning*, vol. 97 of *Proceedings of Machine Learning Research*, 2404–2414 (PMLR, 2019). [arXiv:1905.07488](#).
- [55] Bui, T. D., Yan, J. & Turner, R. E. A unifying framework for gaussian process pseudo-point approximations using power expectation propagation. *Journal of Machine Learning Research* **18**, 3649–3720 (2017). [arXiv:1605.07066](#).
- [56] Pina-Otey, S., Sánchez, F., Gaitan, V. & Lux, T. Likelihood-free inference of experimental neutrino oscillations using neural spline flows. *Phys. Rev. D* **101**, 113001 (2020). [arXiv:2002.09436](#).
- [57] Heinrich, J. Pitfalls of goodness-of-fit from likelihood. In *Proceedings of PHYSTAT2003* (2003).
- [58] Kingma, D. P. & Ba, J. Adam: A Method for Stochastic Optimization. In *International Conference on Learning Representations* (2015). [arXiv:1412.6980](#).
- [59] Bottou, L. Large-scale machine learning with stochastic gradient descent. In *Proceedings of COMPSTAT'2010* (2010).
- [60] Mandt, S., Hoffman, M. D. & Blei, D. M. A variational analysis of stochastic gradient algorithms. In *Proceedings of the 33rd International Conference on Machine Learning*, vol. 48 of *ICML'16*, 354–363 (JMLR.org, 2016). [arXiv:1602.02666](#).
- [61] Blumenson, L. E. A derivation of n-dimensional spherical coordinates. *The American Mathematical Monthly* **67**, 63–66 (1960).
- [62] Kollár, J. Algebraic hypersurfaces. *Bull. Amer. Math. Soc.* **56**, 543–568 (2019). [arXiv:1810.02861](#).